DRAFT VERSION OCTOBER 16, 2014
Preprint typeset using LaTeX style emulateapj v. 5/2/11

arXiv:1407.3833v4 [astro-ph.HE] 14 Oct 2014

RADIATION TRANSPORT FOR EXPLOSIVE OUTFLOWS: OPACITY REGROUPING

RYAN T. WOLLAEGER[1,2] AND DANIEL R. VAN ROSSUM[2]
[1]Department of Nuclear Engineering & Engineering Physics, University of Wisconsin, Madison 1500 Engineering Drive, 410 ERB, Madison, WI, 53706; wollaeger@wisc.edu and
[2]Flash Center for Computational Science, Department of Astronomy & Astrophysics, University of Chicago, Chicago, IL, 60637; daan@flash.uchicago.edu
Draft version October 16, 2014

ABSTRACT

Implicit Monte Carlo (IMC) and Discrete Diffusion Monte Carlo (DDMC) are methods used to stochastically solve the radiative transport and diffusion equations, respectively. These methods combine into a hybrid transport-diffusion method we refer to as IMC-DDMC. We explore a multigroup IMC-DDMC scheme that, in DDMC, combines frequency groups with sufficient optical thickness. We term this procedure "opacity regrouping". Opacity regrouping has previously been applied to IMC-DDMC calculations for problems in which the dependence of the opacity on frequency is monotonic. We generalize opacity regrouping to non-contiguous groups and implement this in `SuperNu`, a code designed to do radiation transport in high-velocity outflows with non-monotonic opacities. We find that regrouping of non-contiguous opacity groups generally improves the speed of IMC-DDMC radiation transport. We present an asymptotic analysis that informs the nature of the Doppler shift in DDMC groups and summarize the derivation of the Gentile-Fleck factor for modified IMC-DDMC. We test `SuperNu` using numerical experiments including a quasi-manufactured analytic solution, a simple ten-group problem, and the W7 problem for Type Ia supernovae. We find that the opacity regrouping is necessary to make our IMC-DDMC implementation feasible for the W7 problem and possibly Type Ia supernova simulations in general. We compare the bolometric light curves and spectra produced by the `SuperNu` and `PHOENIX` radiation transport codes for the W7 problem. The overall shape of the bolometric light curves are in good agreement, as are the spectra and their evolution with time. However, for the numerical specifications we considered, we find that the peak luminosity of the light curve calculated using `SuperNu` is $\sim$10% less than that calculated using `PHOENIX`.

Subject headings: methods: numerical radiative transfer stars: evolution supernovae: general

1. INTRODUCTION

Type Ia supernovae (SNe Ia) are the explosions of Carbon-Oxygen (C-O) white dwarf stars. In the most widely studied model of SNe Ia, a C-O white dwarf approaching the Chandrasekhar mass releases energy from nuclear fusion that exceeds gravitational binding energy of the star, causing the star to explode (Branch & Khokhlov 1995). The resulting high-velocity outflow becomes ballistic in a matter of minutes, and thereafter expands homologously. During this expansion, gamma rays from the radioactive decay of ^{56}Ni heat the outflow, causing it to radiate, with a peak luminosity that can exceed the host galaxy of the supernova.

The majority of observed SNe Ia have similar peak luminosities and spectra (Hillebrandt & Niemeyer 2000). The light curves of most SNe Ia obey a peak luminosity-width relationship (Phillips 1993). As a result, the light curve data for SNe Ia may be fit to a template, enabling its peak luminosity, and therefore its relative distance, to be determined. Consequently, SNe Ia are important "standard candles" for measuring cosmic distances and the expansion rate of the universe, and their use for these purposes led to the discovery of dark energy [see, e.g., Riess et al. (1998); Perlmutter et al. (1999)].

Given the significance of SNe Ia in galaxy formation and evolution (Scannapieco et al. 2008) and in nucleosynthesis, as well as in cosmology, much research has been done to understand how model parameters affect the observable properties of these events; for example, the connection between explosion asymmetry and anomalies in luminosity (Calder et al. 2004; Kromer & Sim 2009). Other research efforts have focused on generating methods, algorithms, and codes that can adequately treat the physics of SNe Ia, along with other hydrodynamic and radiative events in astrophysics. Mihalas & Mihalas (1984, pp. 128,144,160) derived the equations of relativistic fluid flow. Castor (2004, pp. 41,49) describes standard Lagrangian and Eulerian methods to solving hydrodynamic problems. The `FLASH` code (Fryxell et al. 2000; Calder et al. 2002) provides a means of solving the Euler equations for compressive, reactive hydrodynamics with nuclear reactions.

Radiation transport in Type Ia SNe is a complex problem both theoretically and practically. From the theoretical perspective, photons may interact with millions of spectral lines in a heterogeneous material that has multiple ionization states [see, e.g. van Rossum (2012)]. A photon may see an optically thin environment in one location of the outflow and subsequently redshift into resonance with a line opacity elsewhere. Such situations provide a challenge to Local Thermodynamic Equilibrium (LTE) calculations, and especially, Nonlocal Thermodynamic Equilibrium (NLTE) calculations. There is also the question of the leading-order behavior of the radiation at different time scales in the presence of material fluid. Lowrie et al. (2001) make the distinction between the radiation time scale and the fluid time scale as a means of preserving correct relativistic principles in first-order comoving transport.

From the practical perspective, high-fidelity Type Ia SNe simulations are generally seen to be demanding in memory and algorithm efficiency (Baron & Hauschildt 2007). For an end-to-end simulation, one needs to couple a progenitor explosion-phase hydrodynamic simulation to the beginning of the homologous-expansion phase, and then appropriately treat radiation transport in the latter (Seitenzahl et al. 2013; Long et al. 2013). Numerical simulations of the full evolution of the supernova, regardless of the particular explosion model,

involve a large range of densities, temperatures, length scales, time scales, and physical phenomena.

Codes can apply transport theory to the homologous-expansion phase of Type Ia supernovae to synthesize light curves and spectra. Broadly speaking, transport calculations may be performed deterministically with some subset of matrix-solution techniques or stochastically with random-number sampling. The stochastic approach gives terms in the transport equation a probabilistic interpretation; this gives rise to "particles" with sampled properties that can be manipulated and tallied to solve the transport equation. Common methods of computational transport described by Lewis & Miller (1993) include: discrete ordinates (Lewis & Miller 1993, pp. 116,156), integral transport (Lewis & Miller 1993, p. 208), multigroup (Lewis & Miller 1993, p. 61), and finite elements (Adams 2001). The listed methods may be implemented in or in conjunction with Monte Carlo (MC) or deterministic schemes (Urbatsch et al. 1999); the resulting scheme might be deemed a composite method.

Several radiation transport codes have been developed and applied to the W7 model of Nomoto et al. (1984) and to SN Ia models generally. Deterministic codes include PHOENIX, a code based on the iterative, short characteristic method (Hauschildt & Baron 1999; Baron & Hauschildt 2007; Olson & Kunasz 1987). Recently, van Rossum (2012) extended PHOENIX to be able to calculate self-consistently the temporal evolution of the SN Ia outflow. Hauschildt & Wehrse (1991) investigate a discrete ordinates method that incorporates relativistic effects to be able to treat explosive outflow. The MC codes SEDONA of Kasen et al. (2006), the code of Lucy (2005), and the ARTIS code of Kromer & Sim (2009) solve multi-dimensional, time-dependent radiation transport in homologous outflow. Kasen et al. (2006) and Kromer & Sim (2009) solve multifrequency transport by applying the Solobev approximation (Castor 2004, p. 122) to line transport.

Monte Carlo in the context of a velocity field has the favorable property that particles (which are also referred to as packets) may be tracked in one inertial (lab) frame and interact with the fluid in the comoving frame. A particle may have its properties converted to the comoving frame, updated according to the interaction, and converted back to the lab frame if the particle history is not discontinued. Kasen et al. (2006) applies MC iteratively within a time step to obtain converged electron temperatures while Kromer & Sim (2009) find the contribution of MC iteration to be insignificant if small time steps are chosen.

Instead of treating the temperature structure iteratively or explicitly, there exist transport methods that are made fully implicit (N'Kaoua 1991; Brooks 1989) or semi-implicit (Fleck & Cummings 1971; Carter & Forest 1973) through time discretization of the material equation(s) and adjustment of Monte Carlo interpretations (Densmore & Larsen 2004). To our knowledge, these methods have not been extensively examined for application in the SN Ia problem.

Implicit Monte Carlo (IMC) is a stochastic method that may be applied to solve the time-dependent, nonlinear radiation transport equations (Fleck & Cummings 1971; Fleck & Canfield 1984). Of the implicit methods referenced towards the end of the preceding paragraph, IMC is quite possibly the simplest to implement. The IMC method is made semi-implicit through a non-dimensional quantity, referred to as the Fleck factor, that converts a portion of absorption and reemission to instantaneous "effective scattering." [1] By introducing effective scattering, the Fleck factor stabilizes large-time-step [2] radiation transport calculations that might otherwise suffer significant non-physical temperature fluctuations (Fleck & Cummings 1971). However Larsen & Mercier (1987) demonstrate that IMC may still be prone to spurious temperature fluctuation for large time steps and derive a sufficient but not necessary constraint on time step size to prevent non-physical behavior, which they call the "Maximum Principle" (MP). Recent extensions have been made to IMC that mitigate the pathologies associated with the MP [see, e.g., McClarren & Urbatsch (2009); Gentile (2011); McClarren & Urbatsch (2012)].

IMC may suffer in performance when effective scattering dominates over other particle processes. Performance may be improved for calculations having significant physical or effective scattering by combining IMC with either a deterministic or stochastic diffusion method. Stochastic methods include Random Walk (RW) (Fleck & Canfield 1984), Implicit Monte Carlo Diffusion (IMD) (Gentile 2001; Cleveland et al. 2010), and Discrete Diffusion Monte Carlo (DDMC) [see, e.g., Densmore et al. (2007, 2008, 2012)]. The methods listed have been hybridized with IMC and applied to both grey and multifrequency or multigroup problems. Additionally, each method may benefit IMC by replacing small-mean-free-path particle processes with large diffusion processes. The larger diffusion steps of the RW method developed by Fleck & Canfield (1984) place a diffusive particle isotropically on the surface of a sphere of several mean free paths in radius centered at the particle's initial position. This sphere must be bounded by the spatial grid that stores the material properties (Fleck & Canfield 1984). Hence, histories in diffusive domains near cell boundaries will not have sufficiently large displacement spheres; this is found to limit the increase in IMC efficiency (Densmore et al. 2008).

DDMC and IMD differ from RW by discretizing the diffusion equation in space; after some algebra, the resulting terms are given a Monte Carlo interpretation (Densmore et al. 2007; Gentile 2001). The discretization implies that a DDMC particle position within a spatial cell is ambiguous (Wollaeger et al. 2013). IMD discretizes the diffusion equation in time while DDMC keeps particle time continuous. Continuous particle time precludes causal ambiguity for each particle (Densmore et al. 2007).

The hybridization of IMC and DDMC, referred to as IMC-DDMC, has been investigated in multigroup problems (Densmore et al. 2012; Abdikamalov et al. 2012; Wollaeger et al. 2013). In each of the IMC-DDMC implementations, there is a mean-free-path threshold that dictates whether or not a cell and group of the spatial and wavelength grids is amenable to diffusion theory. Densmore et al. (2012) investigate a hybrid for monotonic opacity dependence on frequency that applies grey DDMC in a "large" lower group below a frequency threshold and multifrequency or multigroup IMC above the frequency threshold. Abdikamalov et al. (2012) describe a general multigroup IMC-DDMC scheme for application to neutrino transport in the presence of a fluid; this makes the method velocity dependent. Wollaeger et al. (2013) delineate a velocity-dependent method for photons that reconciles

[1] Note the Fleck factor is not a directly tunable parameter but follows naturally from linearizing the thermal transport equations within each time step.

[2] Roughly speaking, time steps that result in the deposition of a radiation energy density that is greater than or of order the material energy density may cause an IMC simulation to become unstable; hence the pathology depends on the evolution of the radiation field (Gentile 2011).

IMC-DDMC to high-velocity, homologous Lagrangian grids.

Here, we present some extensions to the particular IMC-DDMC method described by Wollaeger et al. (2013). The extensions are opacity regrouping (Densmore et al. 2012) and the Gentile-Fleck factor (Gentile 2011). We implement these features in the IMC-DDMC radiation transport code, `SuperNu` (Wollaeger et al. 2013). We first briefly discuss the thermal radiation transport equations. Then we apply an asymptotic analysis to the continuous, comoving transport equation on an interior of a frequency domain and in a boundary layer of a frequency domain; this clarifies where the DDMC redshift scheme is generally applicable. We summarize standard IMC, the Gentile-Fleck factor modified IMC scheme (Gentile 2011), and the hybrid IMC-DDMC equations. Next, we discuss IMC-DDMC processes and a scheme for combining groups that have DDMC into larger groups to increase computational efficiency. The groups belong to the same spatial cell and must all have opacities that make the cell sufficiently optically thick; this is an optimization since effective scattering for particles in either of the original groups is reduced (Densmore et al. 2012). We term this optimization "opacity regrouping." Opacity regrouping was first implied by Densmore et al. (2012) with a low-frequency DDMC group adaptively adding or subtracting adjacent IMC groups based on the mean free path threshold. Moreover, the extension of the optimization to strongly non-monotonic opacity was anticipated by Densmore et al. (2012). Recently, an opacity regrouping procedure for non-contiguous groups was implemented by Cleveland & Gentile (2014) for Hybrid Implicit Monte Carlo Diffusion (HIMCD); in addition to improving code performance, their approach addresses the effects of teleportation error (Fleck & Canfield 1984) with new method coupling criteria. In addition to the IMC-DDMC mean free path threshold, τ_D, we introduce an additional mean free path threshold, τ_L, that determines regroupable DDMC groups. We investigate the effect of changing regrouping parameters on a simple ten-group problem and the one-dimensional W7 problem presented by Nomoto et al. (1984). Additionally, we explore the effect of a modified Fleck factor, presented by Gentile (2011), on mitigating erroneous fluctuations in the temperature profile in the W7 test problem.

This article is organized as follows. In Section 2, we discuss the approximations to the radiation transport and fluid equations assumed in our code. In Section 3, we perform an asymptotic analysis which indicates a potential source of discrepancy between full multigroup IMC with a discretized Doppler shift correction and continuous-frequency IMC in a multigroup material setting. In Section 4, we describe the Gentile-Fleck factor used in some numerical results and we summarize the IMC-DDMC equations. Additionally, we write the equations for opacity regrouping. In Section 5, we write the formulae used to regroup subsets of groups. In Section 6, we describe IMC-DDMC particle processes including the opacity regrouping and DDMC redshift schemes. In Section 7, we present some calculations that highlight the advantages of the Gentile-Fleck factor and opacity regrouping and demonstrate the application of `SuperNu` to SNe Ia. In Section 7.1, combining the techniques of Oberkampf & Roy (2010) and Gentile (2011), we use a simple quasi-manufactured transport solution for high-velocity outflow to verify the Gentile-Fleck factor's ability to mitigate spurious overheating. In Section 7.2, we demonstrate the improved performance that using DDMC opacity regrouping produces for the multigroup outflow problems presented by Wollaeger et al. (2013). Finally, in Section 7.3, we explore the application of IMC-DDMC with opacity regrouping and the Gentile-Fleck factor to the W7 problem. We also investigate the effects of group opacities that are a composite of Rosseland-like and Planck-like opacities.

2. RADIATION AND FLUID EQUATIONS

We review the underlying theory of the IMC-DDMC scheme tested. Following Pomraning (1973) and Castor (2004), terms in the comoving fluid frame are subscripted with 0. The thermal equation of radiation transport in the lab frame is (Szőke & Brooks 2005; Abdikamalov et al. 2012)

$$\frac{1}{c}\frac{\partial I_\nu}{\partial t} + \hat{\Omega}\cdot\nabla I_\nu + \sigma_{\nu,a} I_\nu = \sigma_{\nu,a} B_\nu - \sigma_{\nu,s} I_\nu + \int_{4\pi}\int_0^\infty \frac{\nu}{\nu'}\sigma_s(\vec{r},\nu'\to\nu,\hat{\Omega}'\to\hat{\Omega}) I_{\nu'}(\vec{r},\hat{\Omega}',t)d\nu' d\Omega' \quad (1)$$

where c is the speed of light, t is time, $\vec{r}$ is the spatial coordinate, $\hat{\Omega}$ is unit direction, ν is frequency, $\sigma_{a,\nu}$ is absorption opacity, $\sigma_{s,\nu}$ is scattering opacity, $\sigma_s(\vec{r},\nu'\to\nu,\hat{\Omega}'\to\hat{\Omega})$ is differential scattering opacity, I_ν is the radiation intensity, and B_ν is the thermal emission source. The first order comoving form of Eq. (1) is (Castor 2004, p. 111)

$$\left(1+\hat{\Omega}_0\cdot\frac{\vec{U}}{c}\right)\frac{1}{c}\frac{DI_{0,\nu_0}}{Dt} + \hat{\Omega}_0\cdot\nabla I_{0,\nu_0} - \frac{\nu_0}{c}\hat{\Omega}_0\cdot\nabla\vec{U}\cdot\nabla_{\nu_0\hat{\Omega}_0} I_{0,\nu_0} + \frac{3}{c}\hat{\Omega}_0\cdot\nabla\vec{U}\cdot\hat{\Omega}_0 I_{0,\nu_0} = \sigma_{0,\nu_0,a}(B_{0,\nu_0} - I_{0,\nu_0}) - \sigma_{0,\nu_0,s} I_{0,\nu_0} + \int_{4\pi}\int_0^\infty \frac{\nu_0}{\nu_0'}\sigma_{0,s}(\vec{r},\nu_0'\to\nu_0,\hat{\Omega}_0'\cdot\hat{\Omega}_0) I_{0,\nu_0'} d\nu_0' d\Omega_0' \ , \quad (2)$$

where $\vec{r}$ is an Eulerian spatial coordinate, $\vec{U}$ is the velocity field, and we have used Castor's notation to denote the photon comoving momentum derivative with $\nabla_{\nu_0\hat{\Omega}_0}$. The homologous flow equation is (Kasen et al. 2006)

$$\vec{r} = \vec{U}t \ , \quad (3)$$

Equation (3) allows for some simplification to material- radiation coupling. The Lagrangian momentum and energy equations, respectively, are

$$\rho\frac{D\vec{U}}{Dt} + \nabla P = -\vec{g} \ , \quad (4)$$

and

$$C_v\frac{DT}{Dt} + P\nabla\cdot\vec{U} = -g^{(0)} \ , \quad (5)$$

where ρ is density, P is fluid pressure, T is fluid temperature, C_v is heat capacity per unit volume, and $(g^{(0)},\vec{g})$ is a radiation energy-momentum coupling 4-vector. Following the justification provided by Kasen et al. (2006) and van Rossum (2012), we neglect P. For the time scales and physical specifications of interest, much more energy is in the radiation field than the material. Incorporating Eq. (3) and $P=0$ into Eqs. (4) and (5)

yields

$$C_v\frac{DT}{Dt} = \int_{4\pi}\int_0^\infty \sigma_{0,\nu_0,a}(I_{0,\nu_0} - B_{0,\nu_0})d\nu_0 d\Omega_0 + \int_{4\pi}\int_0^\infty \sigma_{0,\nu_0,s} I_{0,\nu_0} d\nu_0 d\Omega_0 - \int_{4\pi}\int_0^\infty \int_{4\pi}\int_0^\infty \frac{\nu_0}{\nu_0'}\sigma_{0,s}(\vec{r},\nu_0'\to\nu_0,\hat{\Omega}_0'\cdot\hat{\Omega}_0) I_{0,\nu_0'} d\nu_0' d\Omega_0' d\nu_0 d\Omega_0 = -g_{0,a}^{(0)} - g_{0,s}^{(0)} \quad , \quad (6)$$

where $g_{0,a}^{(0)}$ and $g_{0,s}^{(0)}$ are absorption and scattering contributions to the comoving radiation-material coupling, respectively. Equation (6) is similar in form to the material equation presented by Szőke & Brooks (2005) but with a Lagrangian temporal derivative.

3. DOPPLER SHIFT GROUP EDGE ANALYSIS

Monte Carlo particles may be tracked by either discrete groups or continuous values in frequency space. In the context of relativistic velocity, Doppler shift has an important effect on the radiation intensity's interaction with a group structure. When considering how to track particles through phase space, it is informative to consider approaches to sustaining consistency between multigroup transport and multigroup diffusion. Specifically IMC may have particle frequency tracked and updated continuously in a multigroup setting through explicit changes in reference frame. In contrast, a DDMC particle wavelength is essentially unknown within a group since a DDMC particle step in theory replaces multiple corresponding IMC collision steps. Hence, each time a continuous frequency value is needed from a DDMC particle, it must be sampled from a subgroup distribution (Densmore et al. 2012). DDMC particles may be tracked with continuous frequencies or wavelengths but the values then merely serve as a label for the surrounding group. Consequently, multigroup IMC may simulate the frequency derivative in Eq. (2) exactly while the DDMC scheme described by Wollaeger et al. (2013) can not exactly simulate the frequency derivative. We perform an asymptotic analysis for frequency-dependent, semi-relativistic, comoving transport with the simplification of homologous outflow before considering a group grid that is constant in the comoving frame along with the upwind redshift approximation (Mihalas & Mihalas 1984, p. 475). A group edge of an optically thick region of frequency is treated in a manner analogous to spatial boundary layers (Habetler & Matkowsky 1975; Malvagi & Pomraning 1991). Incorporating Eq. (3) in Eq. (2),

$$\frac{1}{c}\frac{\partial I_{0,\nu_0}}{\partial t} + \hat{\Omega}_0\cdot\nabla I_{0,\nu_0} + \sigma_{0,\nu_0} I_{0,\nu_0} - \frac{\nu_0}{ct}\frac{\partial I_{0,\nu_0}}{\partial \nu_0} + \frac{\vec{r}}{ct}\cdot\nabla I_{0,\nu_0} + \frac{3}{ct} I_{0,\nu_0} = j_{0,\nu_0} \quad , \quad (7)$$

where $\sigma_{0,\nu_0} = \sigma_{0,\nu_0,a} + \sigma_{0,\nu_0,s}$ is isotropic, j_{0,ν_0} is the total source due to scattering and external sources, and the $\hat{\Omega}_0\cdot\vec{U}/c$ term multiplying the Lagrangian derivative has been neglected. Following prior authors (Habetler & Matkowsky 1975; Malvagi & Pomraning 1991), we introduce a parameter, $\varepsilon \ll 1$, and make the following scalings: $c\to c/\varepsilon$, $\sigma_{0,\nu_0}\to\sigma_{0,\nu_0}/\varepsilon$, $\sigma_{0,\nu_0,a}\to\varepsilon\sigma_{0,\nu_0,a}$, $\omega = (\nu-\nu_b)/\varepsilon^m$, $q\to\varepsilon q$, where ν_b is a frequency at boundary b in frequency space and q is the external or thermal source in j_{0,ν_0}. The value m is a number introduced to control the amount of variation in intensity with respect to frequency. If $\partial I_{0,\nu_0}/\partial\omega$ is O(1), then $\partial I_{0,\nu_0}/\partial\nu$ is O($1/\varepsilon^m$). Incorporating the scalings into Eq. (7),

$$\frac{\varepsilon^2}{c}\frac{\partial I_{0,\nu_0}}{\partial t} + \varepsilon\hat{\Omega}_0\cdot\nabla I_{0,\nu_0} + \sigma_{0,\nu_0} I_{0,\nu_0} - \frac{\varepsilon^{2-m}}{ct}\nu_0\frac{\partial I_{0,\nu_0}}{\partial\omega} + \frac{\varepsilon^2}{ct}\vec{r}\cdot\nabla I_{0,\nu_0} + \frac{3\varepsilon^2}{ct} I_{0,\nu_0} = \varepsilon j_{0,\nu_0} \quad , \quad (8)$$

and assuming isotropic elastic scattering,

$$\varepsilon j_{0,\nu_0} = \varepsilon^2\frac{q}{4\pi} + \left(\sigma_{0,\nu_0} - \varepsilon^2\sigma_{0,\nu_0,a}\right)\frac{1}{4\pi}\int_{4\pi} I_{0,\nu_0} d\Omega_0' \quad . \quad (9)$$

For our purposes, we need only consider $m\in\{0,1\}$ for an interior group solution ($m=0$) and a frequency boundary layer solution ($m=1$). The intensity may then be decomposed as $I_{0,\nu_0} = I_i + I_b$ (Malvagi & Pomraning 1991) where I_i is the interior frequency solution and I_b is the boundary layer frequency solution. Moreover, all solutions may be expanded as a power series in ε, $I_{(i,b)} = \sum_{k=0}^\infty I_{(i,b)}^{(k)}\varepsilon^k$. Additionally, we constrain $\lim_{\omega\to\infty} I_b = 0$; this constraint is analogous to the spatial boundary layer constraint of Malvagi & Pomraning (1991) where the value ω would instead correspond to distance away from a surface along a normal vector.

To ensure validity of the stated scalings, we demonstrate the resulting interior solution is the diffusion approximation to the semi-relativistic moment equations presented by Castor (2004, p. 113). The interior intensity is subsequently used along with the boundary layer to obtain the desired result. Setting $m=0$ and incorporating the power series in ε, Eq. (8) may be separated into O(ε^0), O(ε^1), and O(ε^2) equations:

$$I_i^{(0)} = \frac{\phi_i^{(0)}}{4\pi} \quad (10)$$

for O(ε^0),

$$I_i^{(1)} = \frac{\phi_i^{(1)}}{4\pi} - \frac{1}{4\pi}\frac{\hat{\Omega}_0}{\sigma_{0,\nu_0}}\cdot\nabla\phi_i^{(0)} \quad (11)$$

for O(ε^1), and

$$I_i^{(2)} = \frac{1}{4\pi}\left[\frac{q}{\sigma_{0,\nu_0}} + \phi_i^{(2)} - \frac{\sigma_{0,\nu_0,a}}{\sigma_{0,\nu_0}}\phi_i^{(0)} + \frac{\nu_0}{ct\sigma_{0,\nu_0}}\frac{\partial\phi_i^{(0)}}{\partial\nu_0} - \frac{\vec{r}}{ct\sigma_{0,\nu_0}}\cdot\nabla\phi_i^{(0)} - \frac{3}{ct\sigma_{0,\nu_0}}\phi_i^{(0)} - \frac{1}{c\sigma_{0,\nu_0}}\frac{\partial\phi_i^{(0)}}{\partial t} - \frac{\hat{\Omega}_0}{\sigma_{0,\nu_0}}\cdot\nabla\left(\phi_i^{(1)} - \frac{\hat{\Omega}_0}{\sigma_{0,\nu_0}}\cdot\nabla\phi_i^{(0)}\right)\right] \quad (12)$$

for O(ε^2), where Eq. (10) has been used in Eq. (11) and Eqs. (10) and (11) have been used in Eq. (12). The values $\phi_i^{(k)} = \int_{4\pi} I_i^{(m)} d\Omega_0$ are the ε power series coefficients for scalar intensity. Integrating Eq. (12) over comoving solid angle,

$$\frac{1}{c}\frac{\partial\phi_i^{(0)}}{\partial t} - \nabla\cdot\left(\frac{1}{3\sigma_{0,\nu_0}}\nabla\phi_i^{(0)}\right) + \sigma_{0,\nu_0,a}\phi_i^{(0)} - \frac{\nu_0}{ct}\frac{\partial\phi_i^{(0)}}{\partial\nu_0} + \frac{\vec{r}}{ct}\cdot\nabla\phi_i^{(0)} + \frac{3}{ct}\phi_i^{(0)} = q \quad . \quad (13)$$

With some manipulation (by reverting $\vec{r}/t$ to $\vec{U}$ and $3/t$ to $\nabla\cdot\vec{U}$), Eq. (13) can be seen to be the diffusion approximation to the zeroth-moment, frequency-dependent transport equation presented by Castor (2004, p. 113) under the assumptions of isotropic, elastic scattering in the comoving frame and homologous flow.

Next we set $m=1$ and asymptotically analyze the frequency boundary. In the domain examined, the optically thick region will be at higher frequency, or $\omega>0$. Applying the ε power series again, the O(ε^0), O(ε^1), and O(ε^2) equations for I_b are

$$I_b^{(0)}=\frac{\phi_b^{(0)}}{4\pi} \tag{14}$$

for O(ε^0),

$$I_b^{(1)}=\frac{1}{4\pi}\left(\phi_b^{(1)}-\frac{\hat{\Omega}_0}{\sigma_{0,\nu_0}}\cdot\nabla\phi_b^{(0)}+\frac{\nu_b}{ct\sigma_{0,\nu_0}}\frac{\partial\phi_b^{(0)}}{\partial\omega}\right) \tag{15}$$

for O(ε^1), and

$$\begin{aligned}I_b^{(2)}=\frac{1}{4\pi}\Bigg[&\phi_b^{(2)}-\frac{\sigma_{0,\nu_0,a}}{\sigma_{0,\nu_0}}\phi_b^{(0)}+\\&\frac{\nu_b}{ct\sigma_{0,\nu_0}}\frac{\partial\phi_b^{(1)}}{\partial\omega}-\frac{\vec{r}}{ct\sigma_{0,\nu_0}}\cdot\nabla\phi_b^{(0)}-\frac{3}{ct\sigma_{0,\nu_0}}\phi_b^{(0)}\\&-\frac{1}{c\sigma_{0,\nu_0}}\frac{\partial\phi_b^{(0)}}{\partial t}-\frac{\hat{\Omega}_0}{\sigma_{0,\nu_0}}\cdot\nabla\left(\phi_b^{(1)}-\frac{\hat{\Omega}_0}{\sigma_{0,\nu_0}}\cdot\nabla\phi_b^{(0)}\right)\Bigg]\end{aligned} \tag{16}$$

for O(ε^2), where $\phi_b^{(k)}=\int_{4\pi}I_b^{(m)}d\Omega_0$. The term $\partial\phi_b^{(0)}/\partial\omega=0$ from integration of Eq. (16); this is an important result for the remainder of the derivation and has been used in Eqs (15) and (16). If Eq. (16) is integrated, closure for $\phi_b^{(0)}$ is not obtained. In particular, $\partial\phi_b^{(1)}/\partial\omega$ persists. The O(ε^3) solution in terms of $I_b^{(1,2,3)}$ is

$$\begin{aligned}&\frac{1}{c}\frac{\partial I_b^{(1)}}{\partial t}+\hat{\Omega}_0\cdot\nabla I_b^{(2)}+\sigma_{0,\nu_0}I_b^{(3)}-\frac{\nu_b}{ct}\frac{\partial I_b^{(2)}}{\partial\omega}\\&+\frac{\vec{r}}{ct}\cdot\nabla I_b^{(1)}+\frac{3}{ct}I_b^{(1)}=\frac{\sigma_{0,\nu_0}}{4\pi}\phi_b^{(3)}-\frac{\sigma_{0,\nu_0,a}}{4\pi}\phi_b^{(1)}\quad.\end{aligned} \tag{17}$$

To obtain an equation for $\phi_b^{(1)}$, Eq. (16) may be incorporated into the second and fourth terms on the left hand side of Eq. (17) and the overall result may be integrated in Ω_0. Upon integration of $\hat{\Omega}_0\cdot\nabla I_b^{(2)}$, values in Eq. (16) that are even in $\hat{\Omega}_0$ vanish. Upon integration of $\partial I_b^{(2)}/\partial\omega$, values in Eq. (16) that are odd in $\hat{\Omega}_0$ vanish. Fortunately, any terms with $\partial\phi_b^{(0)}/\partial\omega$ vanish as well. The result is

$$\begin{aligned}&\frac{1}{c}\frac{\partial\phi_b^{(1)}}{\partial t}-\nabla\cdot\left(\frac{1}{3\sigma_{0,\nu_0}}\nabla\phi_b^{(1)}\right)+\sigma_{0,\nu_0,a}\phi_b^{(1)}\\&-\frac{\nu_b}{ct}\frac{\partial}{\partial\omega}\left(\frac{\nu_b}{ct\sigma_{0,\nu_0}}\frac{\partial\phi_b^{(1)}}{\partial\omega}\right)+\frac{3}{ct}\phi_b^{(1)}\\&-\frac{\nu_b}{ct}\frac{\partial\phi_b^{(2)}}{\partial\omega}+\frac{\vec{r}}{ct}\cdot\nabla\phi_b^{(1)}=0\quad.\end{aligned} \tag{18}$$

The first and fourth terms in Eq. (18) together resemble a diffusion equation in frequency space. The system of equations is still not closed, but Eq. (17) along with Eq. (18) imply

$$\frac{\partial}{\partial\omega}\left(\frac{\nu_b}{ct\sigma_{0,\nu_0}}\frac{\partial\phi_b^{(1)}}{\partial\omega}\right)=0\quad. \tag{19}$$

Taking $\sigma_{0,\nu_0}=\sigma_{0,\nu_b}$, Eq. (19) solves to

$$\phi_b^{(1)}=\frac{ct\sigma_{0,\nu_0}}{\nu_b}A_1\omega+A_2\quad, \tag{20}$$

where A_1 and A_2 are constant in ω. But $\lim_{\omega\to\infty}\phi_b^{(1)}=0$, so $\phi_b^{(1)}=A_1=A_2=0$. With $\partial\phi_b^{(1)}/\partial\omega=0$, integration of Eq. (16) yields

$$\begin{aligned}&\frac{1}{c}\frac{\partial\phi_b^{(0)}}{\partial t}-\nabla\cdot\left(\frac{1}{3\sigma_{0,\nu_0}}\nabla\phi_b^{(0)}\right)+\sigma_{0,\nu_0,a}\phi_b^{(0)}\\&+\frac{\vec{r}}{ct}\cdot\nabla\phi_b^{(0)}+\frac{3}{ct}\phi_b^{(0)}=0\quad.\end{aligned} \tag{21}$$

Equation (21) indicates the leading-order boundary layer solution has no Doppler correction term when $\partial I_b/\partial\nu$ varies strongly (or $m=1$). Summing Eqs. (13) and (21),

$$\begin{aligned}&\frac{1}{c}\frac{\partial\phi_{0,\nu_0}^{(0)}}{\partial t}-\nabla\cdot\left(\frac{1}{3\sigma_{0,\nu_0}}\nabla\phi_{0,\nu_0}^{(0)}\right)+\sigma_{0,\nu_0,a}\phi_{0,\nu_0}^{(0)}\\&-\frac{\nu_0}{ct}\frac{\partial\phi_i^{(0)}}{\partial\nu_0}+\frac{\vec{r}}{ct}\cdot\nabla\phi_{0,\nu_0}^{(0)}+\frac{3}{ct}\phi_{0,\nu_0}^{(0)}=q\quad.\end{aligned} \tag{22}$$

where $\phi_{0,\nu_0}=\phi_i^{(0)}+\phi_b^{(0)}$ is the uniformly valid leading-order solution. If the interior solution of the upper frequency range is constant in frequency, then

$$\begin{aligned}&\frac{1}{c}\frac{\partial\phi_{0,\nu_0}^{(0)}}{\partial t}-\nabla\cdot\left(\frac{1}{3\sigma_{0,\nu_0}}\nabla\phi_{0,\nu_0}^{(0)}\right)+\sigma_{0,\nu_0,a}\phi_{0,\nu_0}^{(0)}\\&+\frac{\vec{r}}{ct}\cdot\nabla\phi_{0,\nu_0}^{(0)}+\frac{3}{ct}\phi_{0,\nu_0}^{(0)}=q\quad.\end{aligned} \tag{23}$$

The Doppler correction is removed from the leading-order scalar intensity equation in the range of frequencies $\nu_0>\nu_b$ when the leading-order interior solution is constant in frequency. In a piecewise-constant multigroup setting with high-contrast opacities, the intensity can vary significantly between groups and might be treated as constant within groups. Integration of Eq. (23) over a group interval does not produce coupling between groups.

We now extend the analysis to problems with an inelastic scattering component. The extension is a model that serves to provide theoretical evidence that group discretization may have a nontrivial effect on problems with real or effective inelastic scattering (such as those solved with IMC). Densmore (2011) asymptotically analyzes the effect of treating some absorption and re-emission as instantaneous effective scattering while treating the remainder explicitly with a linear spatial sampling distribution. We draw an analogy here between elastic scattering, which preserves ν_0, and IMC effective scattering, which preserves $\vec{r}$. To complete the analogy, inelastic scattering redistributes ν_0 while IMC effective absorption/emission redistributes $\vec{r}$. We now generalize Eq. (7) to include a pedagogical model of inelastic scattering in the diffusive upper frequency range. This inelastic scattering component is meant

to emulate effective scattering in IMC within one group. We rewrite Eq. (7) as

$$\frac{1}{c}\frac{\partial I_{0,\nu_0}}{\partial t}+\hat{\Omega}_0\cdot\nabla I_{0,\nu_0}+\sigma_{0,\nu_0}I_{0,\nu_0} - \frac{\nu_0}{ct}\frac{\partial I_{0,\nu_0}}{\partial \nu_0}+\frac{\vec{r}}{ct}\cdot\nabla I_{0,\nu_0}+\frac{3}{ct}I_{0,\nu_0}=\frac{q}{4\pi}+ \frac{1}{4\pi}(1-\chi)\sigma_s\phi_{0,\nu_0}+\frac{1}{4\pi}\chi\sigma_s p_s(\nu_0)\phi_{0,g} \quad (24)$$

where $\chi \in [0,1]$ is a elastic/inelastic splitting parameter, $p_s(\nu_0)$ is a probability density function, σ_s is a frequency independent scattering opacity coefficient, and $\phi_{0,g} = \int_{\nu_b}^{\nu_t}\phi_{0,\nu_0}d\nu_0$. The value ν_t is the upper bound of the diffusive region. Constraining $\int_{\nu_b}^{\nu_t}p_s(\nu_0)d\nu_0 = 1$, the integral of the total scattering source term over frequency is $\sigma_s\phi_{0,g}$. Considering Eq. (24) implies

$$\int_{4\pi}\int_{\nu_b}^{\nu_t}\frac{\nu_0}{\nu_0'}\sigma_{0,s}(\vec{r},\nu_0'\rightarrow\nu_0,\hat{\Omega}_0'\cdot\hat{\Omega}_0)I_{0,\nu_0'}d\nu_0'd\Omega_0' = \frac{1}{4\pi}(1-\chi)\sigma_s\phi_{0,\nu_0}+\frac{1}{4\pi}\chi\sigma_s p_s(\nu_0)\phi_{0,g} \quad , \quad (25)$$

a consistent differential scattering opacity is

$$\sigma_{0,s}(\vec{r},\nu_0'\rightarrow\nu_0,\hat{\Omega}_0'\cdot\hat{\Omega}_0) = \frac{\sigma_s}{4\pi}\left[(1-\chi)\delta(\nu_0-\nu_0')+\chi\frac{\nu_0'}{\nu_0}p_s(\nu_0)\right] \quad , \quad (26)$$

where $\delta(\nu_0-\nu_0')$ is the Dirac distribution. Thus the total scattering opacity is

$$\sigma_{0,\nu_0,s} = \sigma_s\left[(1-\chi)+\chi\nu_0\int_{\nu_b}^{\nu_t}\frac{p_s(\nu_0')}{\nu_0'}d\nu_0'\right] \quad . \quad (27)$$

Furthermore, we define a secondary distribution,

$$\tilde{p}_s(\nu_0) = \left(\int_{\nu_b}^{\nu_t}\frac{p_s(\nu_0')}{\nu_0'}d\nu_0'\right)^{-1}\frac{p_s(\nu_0)}{\nu_0} \quad , \quad (28)$$

which is shown below to be the $O(\varepsilon^0)$ and $O(\varepsilon^1)$ frequency dependence of scalar intensity. We define $\phi_{i,g}$ and $\phi_{b,g}$ as the interior and boundary scalar intensity group integrated contributions to to the diffusive range. Applying the scalings with $m = 0$, considering the interior solution, and setting $\phi_{0,g} = \sum_{k=0}^{\infty}\phi_{0,g}^{(k)}\varepsilon^k = \sum_{k=0}^{\infty}(\phi_{i,g}^{(k)}+\phi_{b,g}^{(k)})\varepsilon^k$, the $O(\varepsilon^0)$, $O(\varepsilon^1)$, and $O(\varepsilon^2)$ equations for intensity are

$$I_i^{(0)} = \frac{1}{4\pi}\tilde{p}_s(\nu_0)\phi_{i,g}^{(0)} \quad , \quad (29)$$

$$I_i^{(1)} = \frac{1}{4\pi}\tilde{p}_s(\nu_0)\left(\phi_{i,g}^{(1)}-\frac{\hat{\Omega}_0}{\sigma_{0,\nu_0,s}}\cdot\nabla\phi_{i,g}^{(0)}\right) \quad , \quad (30)$$

and

$$I_i^{(2)} = \frac{1}{4\pi}\left[\frac{q}{\sigma_{0,\nu_0,s}}+\frac{\sigma_s}{\sigma_{0,\nu_0,s}}[(1-\chi)\phi_i^{(2)}+\chi p_s(\nu_0)\phi_{i,g}^{(2)}] - \frac{\sigma_{0,\nu_0,a}}{\sigma_{0,\nu_0,s}}\tilde{p}_s(\nu_0)\phi_{i,g}^{(0)}+\frac{\nu_0\phi_{i,g}^{(0)}}{ct\sigma_{0,\nu_0,s}}\frac{\partial\tilde{p}_s}{\partial\nu_0}-\frac{\tilde{p}_s(\nu_0)}{ct\sigma_{0,\nu_0,s}}\vec{r}\cdot\nabla\phi_{i,g}^{(0)} - \frac{3\tilde{p}_s(\nu_0)}{ct\sigma_{0,\nu_0,s}}\phi_{i,g}^{(0)}-\frac{1}{c\sigma_{0,\nu_0,s}}\frac{\partial(\tilde{p}_s(\nu_0)\phi_{i,g}^{(0)})}{\partial t}- \frac{\tilde{p}_s(\nu_0)}{\sigma_{0,\nu_0,s}}\hat{\Omega}_0\cdot\nabla\left(\phi_{i,g}^{(1)}-\frac{\hat{\Omega}_0}{\sigma_{0,\nu_0,s}}\cdot\nabla\phi_{i,g}^{(0)}\right)\right] \quad (31)$$

respectively. Integration of Eq. (31) gives a correct form of the comoving diffusion equation. Additionally, Eq. (31) indicates the Doppler coupling in the diffusion region is dependent on the inelastic scattering profile. The scattering profile determines the leading interior solution. For $m = 1$, the $O(\varepsilon^0)$ and $O(\varepsilon^1)$ equations are

$$I_b^{(0)} = \frac{1}{4\pi}\tilde{p}_s(\nu_b)\phi_{b,g}^{(0)} \quad , \quad (32)$$

$$I_b^{(1)} = \frac{1}{4\pi}\left(\frac{\sigma_s}{\sigma_{0,\nu_0,s}}[(1-\chi)\phi_b^{(1)}+\chi p_s(\nu_b)\phi_{b,g}^{(1)}] - \frac{\hat{\Omega}_0}{\sigma_{0,\nu_0,s}}\cdot\nabla\phi_b^{(0)}+\frac{\nu_b}{ct\sigma_{0,\nu_0,s}}\frac{\partial\phi_b^{(0)}}{\partial\omega}\right) \quad , \quad (33)$$

respectively, where it is assumed the inelastic probability density does not vary strongly in the boundary layer. This assumption may be more clearly expressed as an Taylor expansion of $p_s(\nu)$ around ν_b at a point in the boundary layer: $p_s(\nu) = p_s(\nu_b)+\varepsilon\omega\partial p_s(\nu_b)/\partial\nu$. Equation (32) is frequency independent; so $\partial\phi_b^{(0)}/\partial\omega = 0$. Integration of Eq. (33) over solid angle yields

$$\phi_b^{(1)} = \tilde{p}_s(\nu_b)\phi_{b,g}^{(1)} \quad . \quad (34)$$

Equation (34) implies $\partial\phi_b^{(1)}/\partial\omega = 0$. Invocation of $\partial\phi_b^{(2)}/\partial\omega$ equation was not needed to obtain Eq. (34). The $O(\varepsilon^2)$ boundary layer equation is

$$I_b^{(2)} = \frac{1}{4\pi}\left[\frac{\sigma_s}{\sigma_{0,\nu_0,s}}((1-\chi)\phi_b^{(2)}+\chi p_s(\nu_b)\phi_{b,g}^{(2)})- \frac{\sigma_{0,\nu_0,a}}{\sigma_{0,\nu_0,s}}\phi_b^{(0)}-\frac{\vec{r}}{ct\sigma_{0,\nu_0,s}}\cdot\nabla\phi_b^{(0)}-\frac{3}{ct\sigma_{0,\nu_0,s}}\phi_b^{(0)}- \frac{1}{c\sigma_{0,\nu_0,s}}\frac{\partial\phi_b^{(0)}}{\partial t}-\frac{\hat{\Omega}_0}{\sigma_{0,\nu_0,s}}\cdot\nabla\left(\phi_b^{(1)}-\frac{\hat{\Omega}_0}{\sigma_{0,\nu_0,s}}\cdot\nabla\phi_b^{(0)}\right)\right] \quad . \quad (35)$$

Equation (35) gives a diffusion equation,

$$\frac{1}{c}\frac{\partial\phi_b^{(0)}}{\partial t}-\nabla\cdot\left(\frac{1}{3\sigma_{0,\nu_0,s}}\nabla\phi_b^{(0)}\right)+\sigma_{0,\nu_0,a}\phi_b^{(0)} +\frac{\vec{r}}{ct}\cdot\nabla\phi_b^{(0)}+\frac{3}{ct}\phi_b^{(0)} = \chi\sigma_s\left(p_s(\nu_b)\phi_{b,g}^{(2)}-\frac{p_s(\nu_b)}{\tilde{p}_s(\nu_b)}\phi_b^{(2)}\right) \quad , \quad (36)$$

which has an inelastic scattering source from the O(ε^2) scalar flux. Finally, integrating Eq. (35) over Ω_0, differentiating the result with respect to ω, and using $\partial\phi_b^{(0)}/\partial\omega = \partial\phi_b^{(1)}/\partial\omega = 0$ yields

$$\frac{\partial\phi_b^{(2)}}{\partial\omega} = \frac{(1-\chi)}{(1-\chi)+\chi\nu_b\int_{\nu_b}^{\nu_t}\frac{p_s(\nu_0')}{\nu_0'}d\nu_0'}\frac{\partial\phi_b^{(2)}}{\partial\omega} \quad . \tag{37}$$

If $\chi = 0$, scattering is entirely elastic and Eq. (37) is self-consistent. Otherwise, Eq. (37) is solved with $\partial\phi_b^{(2)}/\partial\omega = 0$ (this may be seen from differentiation of Eq. (36) with respect to ω as well). The uniformly valid diffusion equation is

$$\frac{1}{c}\frac{\partial\phi_{0,\nu_0}^{(0)}}{\partial t} - \nabla\cdot\left(\frac{1}{3\sigma_{0,\nu_0}}\nabla\phi_{0,\nu_0}^{(0)}\right) + \sigma_{0,\nu_0,a}\phi_{0,\nu_0}^{(0)} - \frac{\nu_0\phi_{i,g}^{(0)}}{ct}\frac{\partial\tilde{p}_s}{\partial\nu_0} + \frac{\vec{r}}{ct}\cdot\nabla\phi_{0,\nu_0}^{(0)} + \frac{3}{ct}\phi_{0,\nu_0}^{(0)} = q + \chi\sigma_s\left(p_s(\nu_0)\phi_{0,g}^{(2)} - \frac{p_s(\nu_0)}{\tilde{p}_s(\nu_0)}\phi_{0,\nu_0}^{(2)}\right) \quad . \tag{38}$$

where we have made use of $\sigma_{0,\nu_0} = \sigma_{0,\nu_0,s} +$ O(ε^2). Photon number density is proportional to $\phi_{0,\nu_0}/\nu_0$. Setting $\tilde{\phi} = \phi_{0,\nu_0}^{(0)}/\nu_0$ gives an equation for number density in the comoving frame:

$$\frac{1}{c}\frac{\partial\tilde{\phi}}{\partial t} - \nabla\cdot\left(\frac{1}{3\sigma_{0,\nu_0}}\nabla\tilde{\phi}\right) + \sigma_{0,\nu_0,a}\tilde{\phi} - \frac{\phi_{i,g}^{(0)}}{ct}\frac{\partial\tilde{p}_s}{\partial\nu_0} + \frac{\vec{r}}{ct}\cdot\nabla\tilde{\phi} + \frac{3}{ct}\tilde{\phi} = \frac{q}{\nu_0} + \chi\sigma_s\left(\frac{p_s(\nu_0)}{\nu_0}\phi_{0,g}^{(2)} - \int_{\nu_b}^{\nu_t}\frac{p_s(\nu_0')}{\nu_0'}d\nu_0'\phi_{0,\nu_0}^{(2)}\right) \quad . \tag{39}$$

Integration of Eq. (39) causes the inelastic scattering term on the right hand side to vanish. Consequently, the Doppler correction is again dependent on the interior solution but now also on the scattering distribution, $\tilde{p}_s$. If $\tilde{p}_s = 1/(\nu_t - \nu_b)$, then the comoving photon number density diffusion equation has no Doppler correction term.

The boundary layer solutions do not provide Doppler corrections in the sense described by Castor (2004, p. 112). We thus focus on the Doppler correction that the interior solution provides at the group boundary. Additionally, sufficient inelasticity in collisions, or $\chi \sim$ O(1) in Eq. (24), makes the Doppler correction dependent on the redistribution profile.

To obtain the upwind approximation for Doppler shift in all groups, the transport equation may first be group integrated. We define a frequency grid in the comoving frame with G groups: $\nu_{G+1/2} < \ldots < \nu_{1/2}$. Integrating Eq. (7) over a comoving group, g, yields

$$\frac{1}{c}\frac{\partial I_{0,g}}{\partial t} + \hat{\Omega}_0\cdot\nabla I_{0,g} + \sigma_{0,g}I_{0,g} + \frac{4}{ct}I_{0,g} - \frac{1}{ct}(\nu_{g-1/2}I_{0,\nu_{g-1/2}} - \nu_{g+1/2}I_{0,\nu_{g+1/2}}) + \frac{\vec{r}}{ct}\cdot\nabla I_{0,g} = j_{0,g} \quad , \tag{40}$$

where $I_{0,g} = \int_{\nu_{g+1/2}}^{\nu_{g-1/2}} I_{0,\nu_0}d\nu_0$, $\sigma_{0,g} = \int_{\nu_{g+1/2}}^{\nu_{g-1/2}}\sigma_{0,\nu_0}I_{0,\nu_0}d\nu_0/\int_{\nu_{g+1/2}}^{\nu_{g-1/2}} I_{0,\nu_0}d\nu_0$, and $j_{0,g} = \int_{\nu_{g+1/2}}^{\nu_{g-1/2}} j_{0,\nu_0}d\nu_0$. In practice, $\sigma_{0,g}$, might be computed with an approximation since the exact value is dependent on the solution. Alternatively, one could define the opacity as piecewise constant in frequency. Applying the upwind approximation to the edge frequency-dependent intensity terms yields (Mihalas & Mihalas 1984, p. 475)

$$\frac{1}{c}\frac{\partial I_{0,g}}{\partial t} + \hat{\Omega}_0\cdot\nabla I_{0,g} + \sigma_{0,g}I_{0,g} + \frac{4}{ct}I_{0,g} + \frac{\nu_{g+1/2}}{ct\Delta\nu_g}I_{0,g} + \frac{\vec{r}}{ct}\cdot\nabla I_{0,g} = j_{0,g} + \frac{\nu_{g-1/2}}{ct}\frac{I_{0,g-1}}{\Delta\nu_{g-1}} \quad , \tag{41}$$

where $\Delta\nu_g = \nu_{g-1/2} - \nu_{g+1/2}$. The upwind approximation may be extended trivially to find the multigroup form of Eq. (2). The fifth term on the left hand side and the second term on the right hand side of Eq. (41) are responsible for coupling groups through Doppler shifting. If the group coupling terms in Eq. (41) are removed, then the result describes grey multigroup transport in the context of homologous outflow. If Eq. (41) is solved with a grey MC transport scheme that includes expansion effects (through frame transformations and spatial grid expansion), then a stochastic interpretation must be given to the Doppler shift group coupling terms. The diffusion equation corresponding to Eq. (41) may be found by integrating Eq. (41) over comoving angle and applying Fick's Law,

$$\frac{1}{c}\frac{\partial\phi_{0,g}}{\partial t} - \nabla\cdot\left(\frac{1}{3\sigma_{0,g}}\nabla\phi_{0,g}\right) + \sigma_{0,g}\phi_{0,g} + \frac{4}{ct}\phi_{0,g} + \frac{\nu_{g+1/2}}{ct\Delta\nu_g}\phi_{0,g} + \frac{\vec{r}}{ct}\cdot\nabla\phi_{0,g} = 4\pi j_{0,g} + \frac{\nu_{g-1/2}}{ct\Delta\nu_{g-1}}\phi_{0,g-1} \quad , \tag{42}$$

where opacities have been assumed piecewise constant in frequency. The Doppler correction terms in Eqs. (41) and (42) can be interpreted as "Doppler shift opacities", where sampling the value $\nu_{g+1/2}/ct\Delta\nu_g$ would induce a particle to transition from group g to group $g+1$. If an IMC particle samples a Doppler shift event, the particle's frequency will be updated to an adjacent group.

Instead of assuming a fully grouped approach, we implement a Doppler shift scheme in IMC-DDMC that more closely emulates continuous frequency transport in the presence of piecewise constant opacities. We make the constraint in our code that inelastic redistribution at the subgroup level is uniform, or

$$p_s(\nu_0) = \frac{1}{\Delta\nu_g} \quad . \tag{43}$$

Considering Eqs. (28), and (29): $\tilde{p}_s \sim 1/\nu \sim \phi_i^{(0)}$, and the Doppler correction in Eq. (38) and (39) satisfies

$$-\frac{\nu_0\phi_{i,g}^{(0)}}{ct}\frac{\partial\tilde{p}_s}{\partial\nu_0} = \frac{1}{ct}\phi_i^{(0)} \quad . \tag{44}$$

Since the equations for scalar flux in the frequency boundary layer have no Doppler correction, we assume $I_b = 0$; the interior radiation field thus account for all radiation in the diffusive frequency region. Then the entire radiation field has the Doppler correction. Consequently, incorporating Eq. (44) into Eq. (38), neglecting higher order scattering terms, assuming piecewise constant opacities and integrating over the group

range yields

$$\frac{1}{c}\frac{\partial \phi^{(0)}_{0,g}}{\partial t} - \nabla\cdot\left(\frac{1}{3\sigma_{0,g}}\nabla\phi^{(0)}_{0,g}\right) + \sigma_{a,g}\phi^{(0)}_{0,g} + \frac{\vec{r}}{ct}\cdot\nabla\phi^{(0)}_{0,g} + \frac{4}{ct}\phi^{(0)}_{0,g} = q_g \quad . \tag{45}$$

Equation (45) is Eq. (42) without upwind Doppler shift terms. We infer that the degree of elasticity (in our model χ) is important to how DDMC groups redshift to other groups, particularly when DDMC emulates continuous frequency transport. In order to have Eq. (45) represent grey diffusion for the case of one group, we limit Doppler shift of particles to adjacent groups for problems with inelastic-dominant collisions, or $\chi \sim$ O(1). Such a constraint should emulate IMC for problems with inelastic-dominant collisions. Assuming a non-zero velocity field exists and inelastic opacity is large with respect to $\nu_{g+1/2}/ct\Delta\nu_g$, IMC particles would have their frequencies redistributed many times before streaming to the edge of a group; this may greatly reduce the occurrence of Doppler shift between groups in IMC. In Section 6, we describe a DDMC Doppler shift scheme that takes into account the degree of inelasticity in collisions.

4. MULTIGROUP IMC-DDMC EQUATIONS

Equation (6) is amenable to the semi-implicit time difference described by Fleck & Cummings (1971). Moreover, the semi-implicit discretization procedure may be applied on Eqs. (2) and (6) to obtain IMC equations for the comoving frame. The multigroup form of Eq. (6) is

$$C_v\frac{DT}{Dt} = \sum_{g=1}^{G}\int_{4\pi}\sigma_{a,g}I_{0,g}d\Omega_0 - c\sigma_P aT^4 - g^{(0)}_{0,s} \tag{46}$$

where $\sigma_{a,g}$ is comoving grouped absorption opacity, σ_P is comoving Planck opacity, and we have compressed the notation of the inelastic scattering contribution since it is a material source with a treatment described by Fleck & Cummings (1971). Introducing a parameter $\beta = 4aT^3/C_v$ and integrating Eq. (46) over a time step gives

$$(aT^4)_{n+1} - (aT^4)_n = \int_{t_n}^{t_{n+1}}\beta\left(\sum_{g=1}^{G}\int_{4\pi}\sigma_{a,g}I_{0,g}d\Omega_0 - c\sigma_P aT^4 - g^{(0)}_{0,s}\right)dt \quad , \tag{47}$$

where a value subscripted with n implies evaluation at the beginning of a time step indexed by n. IMC is made semi-implicit and linear within a time step by setting $\beta = \beta_n$, $\sigma_{a,g} = \sigma_{a,g,n}$, and $\sigma_P = \sigma_{P,n}$ (Fleck & Cummings 1971; Fleck & Canfield 1984). Additionally, setting $\Delta t_n\bar{I}_{0,g} = \int_{t_n}^{t_{n+1}} I_{0,g}dt$, $\Delta t_n[\alpha T^4_{n+1} + (1-\alpha)T^4_n] = \int_{t_n}^{t_{n+1}} T^4$, and $\Delta t_n\bar{g}^{(0)}_{0,s} = \int_{t_n}^{t_{n+1}} g^{(0)}_{0,s}dt$ gives

$$aT^4_{n+1} - aT^4_n = \beta_n\Delta t_n\sum_{g=1}^{G}\int_{4\pi}\sigma_{a,g,n}\bar{I}_{0,g}d\Omega_0 - c\Delta t_n\beta_n\sigma_{P,n}[\alpha aT^4_{n+1} + (1-\alpha)aT^4_n] - \Delta t_n\beta_n\bar{g}^{(0)}_{0,s} \tag{48}$$

where $\Delta t_n = t_{n+1} - t_n$ and $\alpha \in [0,1]$ is the standard IMC time centering parameter. With Eq. (48), an expression may be found for $\alpha aT^4_{n+1} + (1-\alpha)aT^4_n$ that excludes T_{n+1}. Introducing the Fleck factor,

$$f_n = \frac{1}{1+\alpha\beta_n c\Delta t_n\sigma_{P,n}} \quad , \tag{49}$$

the time centered aT^4 is (Abdikamalov et al. 2012)

$$\alpha aT^4_{n+1} + (1-\alpha)aT^4_n = \frac{1}{c\sigma_{P,n}}(1-f_n)\sum_{g=1}^{G}\int_{4\pi}\sigma_{a,g,n}\bar{I}_{0,g}d\Omega_0 + f_n aT^4_n - \frac{1}{c\sigma_{P,n}}(1-f_n)\bar{g}^{(0)}_{0,s} \quad . \tag{50}$$

By replacing $\bar{I}_{0,g}$ with $I_{0,g}$, the thermal emission source term for a group g in the comoving transport equation may be approximated as

$$\sigma_{a,g,n}B_{0,g} = \frac{1}{4\pi}caT^4\sigma_{a,g,n}b_{g,n} = (1-f_n)\frac{\sigma_{a,g,n}b_g}{4\pi\sigma_P}\sum_{g'=1}^{G}\int_{4\pi}\sigma_{a,g',n}\bar{I}_{0,g'}d\Omega_0 + \frac{\sigma_{a,g,n}b_{g,n}}{4\pi\sigma_{P,n}}f_n acT^4_n - (1-f_n)\frac{\sigma_{a,g,n}b_{g,n}}{4\pi\sigma_{P,n}}\bar{g}^{(0)}_{0,s} \quad . \tag{51}$$

Equations (47)-(51) are not the only way to semi-implicitly discretize the temperature equation in time. Moreover, in certain circumstances it may be appropriate to apply different approximations in order to avoid problematic IMC errors. In particular, Larsen & Mercier (1987) derive a "Maximum Principle" for IMC that supplies a sufficient but not necessary upper bound on time step sizes. It follows from their analysis that IMC is not guaranteed to give a physical result for any possible numerical setup. If IMC numerical parameters are ill-conditioned, spurious temperature oscillations and overheating may occur (McClarren & Urbatsch 2012). Gentile (2011) performs a similar discretization but linearly expands opacity and aT^4 from their values at n to values at $n+1$. Despite severe approximations (Gentile 2011), the result is a modified Fleck factor that adapts to the state of the radiation field. Instead of expanding material quantities in T, an alternative approach to obtaining the result of Gentile (2011) is to make a change of variables in the time derivative similar to that of Fleck & Cummings (1971). Defining

$$E_* = \frac{1}{c\Delta t_n\bar{\sigma}_P}\int_{t_n}^{t_{n+1}}\sum_{g=1}^{G}\int_{4\pi}\sigma_{a,g}I_{0,g}d\Omega_0 dt \quad , \tag{52}$$

where $\bar{\sigma}_P$ is time centered, Equation (46) may be stated as

$$\frac{1}{\sigma_P\tilde{\beta}}\frac{D}{Dt}[\sigma_P(aT^4 - E_*)] = \sum_{g=1}^{G}\int_{4\pi}\sigma_{a,g}I_{0,g}d\Omega_0 - c\sigma_P aT^4 - g^{(0)}_{0,s} \quad , \tag{53}$$

where

$$\tilde{\beta} = \frac{1}{C_v}\left[4aT^3 + (aT^4 - E_*)\frac{1}{\sigma_P}\frac{\partial\sigma_P}{\partial T}\right] \quad . \tag{54}$$

Evaluating $\sigma_P\tilde{\beta}$ on the left hand side of Eq. (53) at the beginning of a time step, integrating Eq. (53) with respect to time, setting $\int_{t_n}^{t_{n+1}} \sigma_P a T^4 = \Delta t_n[\alpha\sigma_{P,n+1}aT_{n+1}^4 + (1-\alpha)\sigma_{P,n}aT_n^4]$, setting $\bar{\sigma}_P = \alpha\sigma_{P,n+1} + (1-\alpha)\sigma_{P,n}$, and setting $\Lambda_{a,n} = \sigma_{P,n}(aT_n^4 - E_*)$ give

$$\Lambda_{a,n+1} - \Lambda_{a,n} = c\Delta t_n \sigma_{P,n}\tilde{\beta}_n\left(-\alpha\Lambda_{a,n+1} - (1-\alpha)\Lambda_{a,n} - \bar{g}_{0,s}^{(0)}\right) \quad . \tag{55}$$

Defining the Gentile-Fleck factor as

$$\tilde{f}_n = \frac{1}{1+\alpha\tilde{\beta}_n c\Delta_t\sigma_{P,n}} \quad , \tag{56}$$

The time centered emission term is found to be

$$\alpha\sigma_{P,n+1}aT_{n+1}^4 + (1-\alpha)\sigma_{P,n}aT_n^4 = \tilde{f}_n\sigma_{P,n}aT_n^4 - (1-\tilde{f}_n)\bar{g}_{0,s}^{(0)} + \bar{\sigma}_P\left(1 - \frac{\sigma_{P,n}}{\bar{\sigma}_P}\tilde{f}_n\right)E_* \quad . \tag{57}$$

The next simplification is $\sigma_{P,n}/\bar{\sigma}_P$ in the last term on the right hand side of Eq. (57). By incorporating Eq. (52) for E_*, Eq. (52) may be a substitute for the emission term in the comoving thermal transport equation. The value $\tilde{f}_n$ may be interpreted in the same manner as f_n to control the amount of effective scattering and absorption in IMC. Unfortunately, the form of $\tilde{\beta}_n$ allows $\tilde{f}_n$ to be negative. Gentile (2011) constrains $\tilde{f}_n \in [0,1]$ by setting

$$\tilde{\beta}_n = \frac{1}{C_v}\left[4aT_n^3 + \max\left((aT_n^4 - E_*)\frac{1}{\sigma_{P,n}}\left.\frac{\partial\sigma_P}{\partial T}\right|_{T_n}, 0\right)\right] \tag{58}$$

Additionally, E_* is estimated with the tallied radiation energy density from time step $n-1$. Equations (56) and (58) are the exact same equations for the modified Fleck factor derived by Gentile (2011). If the Planck opacity decreases with temperature and the radiation temperature is higher than the material temperature, then $\tilde{\beta}_n > \beta_n$ and $\tilde{f}_n < f_n$. From Eq. (58), it is evident that $\tilde{f}_n \leq f_n$ and the Gentile-Fleck factor always increases effective scattering over the standard Fleck factor (Gentile 2011). Unfortunately, the cost of more stability in IMC temperature update is a decrease in IMC efficiency. However, hybridizing IMC with a diffusion scheme mitigates the added cost (Gentile 2011).

It remains to assess whether or not such a modification to IMC is needed for problems like the W7 SN Ia described by Nomoto et al. (1984). The grey form of the Maximum Principle of Larsen & Mercier (1987) is

$$\Delta t_n\left[ac\sup_{T_L<T<T_U}\left\{\frac{\sigma_P}{C_v}\left(\frac{T_U^4 - T^4}{T_U - T} - 4\alpha T^3\right)\right\}\right] \leq 1 \quad , \tag{59}$$

where T_L and T_U are physical lower and upper bounds on temperature. To reiterate the grey Maximum Principle, Eq. (59), provides a sufficient time step limit but is not necessary (Larsen & Mercier 1987). Larsen & Mercier (1987) prove the general form of the IMC Maximum Principle by induction over the grid of time steps n. If $T_L \leq T_n \leq T_U$ and $B_{0,\nu_0}(T_L) \leq I_{0,\nu_0,n} \leq B_{0,\nu_0}(T_U)$ then $T_L \leq T_{n+1} \leq T_U$ and $B_{0,\nu_0}(T_L) \leq I_{0,\nu_0,n+1} \leq B_{0,\nu_0}(T_U)$ if there is no external source of radiation or material energy. For $\sigma_P/\rho = 0.13$ cm^2/g, $C_v/\rho = 2.0\times10^7$, $T_U = 100000$ K, and $T_L = 10000$ K, the grey Maximum Principle gives $\Delta t_n \leq 0.6$ milliseconds. The nominal opacity and heat capacity are from the analytic SN Ia analysis performed by Pinto & Eastman (2000). W7 results in Section 7 indicate the modified Fleck factor derived by Gentile (2011) mitigates temperature instabilities in outer spatial cells at late time in the SN evolution.

For the remainder of this section (Section 4), we will write down the IMC-DDMC equations with f_n but note that modified IMC-DDMC merely replaces f_n with $\tilde{f}_n$. The multigroup, semi-relativistic IMC equations in differential form are

$$C_v\frac{DT}{Dt} = f_n\sum_{g=1}^{G}\int_{4\pi}\sigma_{a,g}I_{0,g}d\Omega_0 - f_n\sigma_P caT^4 - g_{0,s}^{(0)} \quad , \tag{60}$$

and (Castor 2004, p. 112)

$$\begin{aligned}
&\left(1 + \hat{\Omega}_0\cdot\frac{\vec{U}}{c}\right)\frac{1}{c}\frac{DI_{0,g}}{Dt} + \hat{\Omega}_0\cdot\nabla I_{0,g} \\
&+ \frac{4}{c}\hat{\Omega}_0\cdot\nabla\vec{U}\cdot\hat{\Omega}_0 I_{0,g} - \frac{1}{c}\hat{\Omega}_0\cdot\nabla\vec{U}\cdot(\mathbf{I} - \hat{\Omega}_0\hat{\Omega}_0)\cdot\nabla_{\hat{\Omega}_0}I_{0,g} \\
&- \frac{1}{c}\hat{\Omega}_0\cdot\nabla\vec{U}\cdot\hat{\Omega}_0\left(\nu_{g-1/2}I_{0,\nu_{g-1/2}} - \nu_{g+1/2}I_{0,\nu_{g+1/2}}\right) \\
&+ (\sigma_{s,g,n} + \sigma_{a,g,n})I_{0,g} = \frac{f_n}{4\pi}\sigma_{a,g,n}b_{0,g,n}acT_n^4 \\
&+ \frac{b_{0,g,n}\sigma_{a,g,n}}{4\pi\sigma_{P,n}}(1-f_n)\sum_{g'=1}^{G}\int_{4\pi}\sigma_{a,g',n}I_{0,g'}d\Omega_0' \\
&+ \int_{\nu_{g+1/2}}^{\nu_{g-1/2}}\int_{4\pi}\int_0^\infty\frac{\nu_0}{\nu_0'}\sigma_{s,n}(\vec{r},\nu_0'\to\nu_0,\hat{\Omega}_0'\cdot\hat{\Omega}_0)\times \\
&\qquad I_{0,\nu_0'}d\nu_0'd\Omega_0'd\nu_0 \quad ,
\end{aligned} \tag{61}$$

where $g_{0,s}^{(0)}$ has been grouped back into the material equation, Eq. (61). Following Abdikamalov et al. (2012), Eq. (61) may be integrated in Ω_0 and operator split into a transport component, a Doppler shift component, and an advection-expansion component. Fick's Law may be applied to the transport component to obtain a diffusion equation. To obtain a DDMC equation, the diffusion component is discretized in space to obtain "leakage opacities" (Densmore et al. 2007) which determine the likelihood of a DDMC particle moving to an adjacent cell. The DDMC equation is hybridized with solutions to the IMC equation in space and frequency through an asymptotic diffusion limit boundary condition and effective scattering, respectively (Densmore et al. 2007, 2012; Abdikamalov et al. 2012; Wollaeger et al. 2013). The operator-split Doppler-shift and advection-expansion equations are

$$\left(\frac{\partial\phi_{0,g}}{\partial t}\right)_{\text{Doppler}} + \frac{\nabla\cdot\vec{U}}{3}\phi_{0,g} = \frac{\nabla\cdot\vec{U}}{3}\left(\nu_{g-1/2}\phi_{0,\nu_{g-1/2}} - \nu_{g+1/2}\phi_{0,\nu_{g+1/2}}\right) \quad , \tag{62}$$

and

$$\left(\frac{\partial\phi_{0,g}}{\partial t}\right)_{\text{Adv/Exp}} + \nabla\cdot(\vec{U}\phi_{0,g}) = 0 \quad , \tag{63}$$

respectively, where $\phi_{0,g} = \int_{4\pi} I_{0,g} d\Omega_0$. Neglecting physical inelastic scattering, on a spatial domain indexed by $j \in \{1 \dots J\}$, the hybrid DDMC component of the operator split is (Densmore et al. 2012; Wollaeger et al. 2013)

$$\begin{aligned}
&\frac{1}{c}\frac{\partial \phi_{0,j,g}}{\partial t} + \left(\sum_{j'} \tilde{\sigma}_{j\to j',g} + (1-\gamma_{j,g,n})(1-f_{j,n})\sigma_{a,j,g,n} \right. \\
&\left. + f_{j,n}\sigma_{a,j,g,n} \right) \phi_{0,j,g} = f_{j,n}\gamma_{j,g,n}\sigma_{P,j,n} a c T_{j,n}^4 \\
&+ \frac{1}{V_j} \sum_{j'} V_{j'} \sum_{g'_D} \frac{b_{j',g\leftrightarrow g'_D,n}}{b_{j',g,n}} \sigma_{j'\to j,g'_D} \phi_{0,j',g'_D} \\
&+ \frac{1}{V_j} \sum_{j'} \sum_{g'_T} \int_{A_{b(j,j')}} \int_{\hat{\Omega}_0\cdot\vec{n}<0} \int_{g\leftrightarrow g'_T} G_{\vec{U},b(j,j')}(|\hat{\Omega}_0\cdot\vec{n}|) \times \\
&P_{b(j,j')}(|\hat{\Omega}_0\cdot\vec{n}|) |\hat{\Omega}_0\cdot\vec{n}| I_{0,\nu_0} d\nu_0 d\Omega_0 d^2\vec{r} \\
&+ \frac{\gamma_{j,g,n}(1-f_{j,n})}{V_j} \times \\
&\sum_{g_T} \int_{V_j} \int_{4\pi} \int_{\nu_{g_T+1/2}}^{\nu_{g_T-1/2}} \sigma_{0,\nu_0,a,j,n} I_{0,\nu_0} d\nu_0 d\Omega_0 d^3\vec{r} \\
&+ \gamma_{j,g,n}(1-f_{j,n}) \sum_{g_D} \sigma_{a,j,g_D,n} \phi_{0,j,g_D} \qquad (64)
\end{aligned}$$

where the subscript j indicates a finite volume or spatially piecewise-constant evaluation, $\tilde{\sigma}_{j\to j',g}$ is the leakage opacity for particle transition from cell j to j', $\gamma_{j,g,n} = b_{j,g,n}\sigma_{a,j,g,n}/\sigma_{P,j,n}$, $(1-\gamma_{j,g,n})(1-f_{j,n})\sigma_{a,j,g,n}$ is the effective scattering opacity for scattering out of group g, V_j is the volume of cell j, g_D (g_T) are group indexes in cell j that are DDMC (IMC), $b_{j',g\leftrightarrow g'_D,n}$ is the integral of the normalized Planck function evaluated at $T_{j'}$ and integrated over the intersection in frequency of the current group, g, and a diffusion group in cell j', g'_D. Furthermore, $A_{b(j,j')}$ indicates the area of spatial interface between an IMC cell j' and the current cell j, $\vec{n}$ is a unit vector normal to surface $A_{b(j,j')}$ pointing from the interior of cell j, $G_{\vec{U},b(j,j')}(\mu) \approx 1 + (2/c)\vec{n}\cdot\vec{U}(\vec{r}_b,t)(0.55/\mu - 1.25\mu)$ is a particle weight modification factor for semi-relativistic boundaries (Wollaeger et al. 2013), and $P_{b(j,j')}$ is the probability of IMC to DDMC particle transition corresponding to the asymptotic diffusion limit boundary condition (Densmore et al. 2008; Malvagi & Pomraning 1991). The $\sim$ notation over the leakage opacity indicates it may be a composite of leakage opacities for DDMC to IMC transitions and DDMC to DDMC transitions. The form of the leakage opacity is (Densmore et al. 2012)

$$\begin{aligned}
&\tilde{\sigma}_{j\to j',g} = \\
&\left(\frac{\sum_{g'_D} b_{j,g\leftrightarrow g'_D,n}}{b_{j,g,n}} \right) \sigma_{j\to j',g} + \left(\frac{\sum_{g'_T} b_{j,g\leftrightarrow g'_T,n}}{b_{j,g,n}} \right) \sigma_{b(j,j'),g}
\end{aligned} \qquad (65)$$

where $\sigma_{j\to j',g}$ is the leakage opacity to DDMC groups and $\sigma_{b(j,j'),g}$ is the leakage opacity to IMC groups in cell j'. The pure leakage opacities may themselves be weighted averages of leakage opacities corresponding to $(j,g) \to (j',g'_D)$ and $(j,g) \to (j',g'_T)$ transitions. A resolved form of Eq. (65) is

$$\begin{aligned}
\tilde{\sigma}_{j\to j',g} = &\left(\frac{\sum_{g'_D} b_{j,g\leftrightarrow g'_D,n} \sigma_{j\to j',g\to g'_D}}{b_{j,g,n}} \right) \\
&+ \left(\frac{\sum_{g'_T} b_{j,g\leftrightarrow g'_T,n} \sigma_{b(j,j'),g\to g'_T}}{b_{j,g,n}} \right)
\end{aligned} \qquad (66)$$

where the form of $\sigma_{j\to j',g}$ and $\sigma_{b(j,j'),g}$ may be solved for in Eq. (66) from Eq. (65).

5. OPACITY REGROUPING

Opacity regrouping is an optimization of DDMC that may be incorporated into Eq. (64) without having to modify the form of the equation. The process involves combining DDMC frequency intervals and properties corresponding to DDMC frequency intervals to make larger groups. This scheme was devised by Densmore et al. (2012) as an approximation of an adaptive threshold frequency between grey DDMC and multigroup IMC. Since the set of groups is divided into a DDMC set and an IMC set, the DDMC groups corresponding to a set of frequency intervals do not have to match the set of IMC groups corresponding to the same set of frequency intervals. Equation (64) accommodates adaptive grouping, unaligned groups at spatial boundaries, and opacity regrouping.

To illustrate the opacity regrouping process, we consider a subset with subindex $l \in \{1 \dots L\}$ of a resolved group structure. Groups that satisfy given regrouping criteria belong to the subset and form a group denoted $\cup_{l=1}^{L} g_l$. The union $\cup_{l=1}^{L}$ implies a union of the frequency intervals for each group index g_l. The regrouped absorption opacity is set to

$$\sigma_{a,j,\cup_l g_l,n} = \frac{\sum_{l=1}^{L} b_{j,g_l,n}\sigma_{a,j,g_l,n}}{\sum_{l=1}^{L} b_{j,g_l,n}} \quad . \qquad (67)$$

Similarly, the regrouped leakage opacity is

$$\tilde{\sigma}_{j\to j',\cup_l g_l} = \frac{\sum_{l=1}^{L} b_{j,g_l,n}\tilde{\sigma}_{j\to j',g_l}}{\sum_{l=1}^{L} b_{j,g_l,n}} \quad . \qquad (68)$$

Incorporating Eq. (66) into Eq. (68) yields

$$\begin{aligned}
\tilde{\sigma}_{j\to j',\cup_l g_l} = &\left(\sum_{l=1}^{L} b_{j,g_l,n} \right)^{-1} \times \\
&\sum_{l=1}^{L} \left[\sum_{g'_D} b_{j,g_l\leftrightarrow g'_D} \sigma_{j\to j',g_l\to g'_D} + \right. \\
&\left. \sum_{g'_T} b_{j,g_l\leftrightarrow g'_T,n} \sigma_{b(j,j'),g_l\to g'_T} \right] \quad . \qquad (69)
\end{aligned}$$

If a leakage event from $\cup_{l=1}^{L} g_l$ is sampled, the probability of leaking to an interfacing group g'_D is $(\tilde{\sigma}_{j\to j',\cup_l g_l} \sum_{l=1}^{L} b_{j,g_l,n})^{-1} \sum_{l=1}^{L} b_{j,g_l\leftrightarrow g'_D} \sigma_{j\to j',g_l\to g'_D}$. The regrouped term responsible for the increase in efficiency over DDMC without regrouping is

$$\gamma_{j,\cup_l g_l,n} = \sum_{l=1}^{L} \gamma_{j,g_l,n} \quad , \qquad (70)$$

which reduces overall effective scattering since a DDMC particle in g_l may no longer scatter to $g_{l'}$ if these groups are in $\cup_{l=1}^{L} g_l$. Equations (67)-(70) may be used in place of the non-opacity-regrouped (non-OR) counterparts in Eq. (64) to solve Eq. (64) for a regrouped intensity, $\phi_{0,j,\cup_l g_l}$. The values indexed by g_D in the last term on the right hand side of Eq. (64) correspond to DDMC groups not used to construct $\cup_{l=1}^{L} g_l$.

The cost of regrouping opacities is a loss in accuracy of the distribution of the radiation field over the groups. However, the use of the Planck function in weighting the group quantities for regrouping may suffice when effective scattering is a dominant interaction.

6. IMC AND DDMC PROCESSES

We now summarize the MC implementation of the equations from Section 4 for a homologous outflow. Following Lucy (2005) and Abdikamalov et al. (2012), IMC particles are streamed in a lab frame and converted to the fluid frame when a collision is sampled. To first order in $\vec{U}/c$, IMC particle lab-frame frequency and direction may be expressed in terms of their comoving counterparts as (Castor 2004, p. 104)

$$\nu = \nu_0 \left(1 + \frac{\hat{\Omega}_0 \cdot \vec{U}}{c}\right) \quad , \tag{71}$$

and

$$\hat{\Omega} = \frac{\hat{\Omega}_0 + \vec{U}/c}{1 + \hat{\Omega}_0 \cdot \vec{U}/c} \quad . \tag{72}$$

Equations (71) and (72) account for Doppler shift and aberration, respectively (Lucy 2005). An opacity σ_0 transforms to a lab frame value, σ, with $\sigma = \nu_0 \sigma_0 / \nu$ (Castor 2004, p. 106). Equation (71) may be used to express opacity in terms of direction.

Despite occurring in a moving spatial grid, MC processes may be tracked over an unchanging "velocity grid" (Kasen et al. 2006; Wollaeger et al. 2013). The collision and census IMC velocity distances computed tracking a particle, labeled p, with coordinate $(t_p, \vec{U}_p)$ in cell j, in time step n, and group g are (Wollaeger et al. 2013)

$$u_{\text{col}} = \frac{-\ln(\xi)}{t_n(1 - \hat{\Omega}_p \cdot \vec{U}/c)((1-f_n)\sigma_{a,j,g,n} + \sigma_{s,j,g,n})} \quad , \tag{73}$$

$$u_{\text{cen}} = c\frac{1}{t_n}(t_n + \Delta t_n - t_p) \quad , \tag{74}$$

respectively, where $\xi \in (0,1]$ is a uniformly sampled random variable. Eq. (73) assumes effective absorption is treated exactly during streaming. The velocity distance to the boundary of cell j is geometry dependent. For one dimensional spherical geometry the velocity distance to a boundary is

$$u_b = \begin{cases} |(U_{j-1/2}^2 - (1-\mu_p^2)U_p^2)^{1/2} + \mu_p U_p| \\ \quad \text{if } \mu_p < -\sqrt{1 - (U_{j-1/2}/U_p)^2} \\ (U_{j+1/2}^2 - (1-\mu_p^2)U_p^2)^{1/2} - \mu_p U_p \\ \quad \text{otherwise} \end{cases} \tag{75}$$

where $\mu_p = \hat{\Omega}_p \cdot \vec{U}_p / |\vec{U}_p|$. A distance required for an IMC particle to stream into another group through Doppler shift may be incorporated. In spherical coordinates, the distance to redshift between groups is (Wollaeger et al. 2013)

$$u_{\text{Dop}} = c\left(1 - \frac{\nu_{g+1/2}}{\nu_p}\right) - \vec{U}_p \cdot \hat{\Omega}_p \tag{76}$$

for continuous frequency transport. Converting ν_p from the lab frame to the fluid frame, $\nu_{0,p}$, in Eq. (76) yields $u_{\text{Dop}} = c(1 - \nu_{g+1/2}/\nu_{0,p})(1 - \vec{U}_p \cdot \hat{\Omega}_p/c)$. Since $\nu_{0,p} \geq \nu_{g+1/2}$ and $\vec{U}_p \cdot \hat{\Omega}_p / c < 1$, $u_{\text{Dop}} \geq 0$.

Each IMC particle has its spatial coordinate stored after transport. Thus, the velocity coordinate of each IMC particle must be updated before or after a transport step (Wollaeger et al. 2013). If a DDMC region advects into an IMC particle, the IMC particle is placed on the cell surface so that the IMC-DDMC interface condition may be applied in the subsequent transport phase.

In DDMC, Eqs. (62), (63) and (64) determine appropriate modifications to DDMC particle properties. Eq. (64) has no velocity terms and may be solved with static material DDMC (Abdikamalov et al. 2012). Equation (62) determines the Doppler correction to a particle energy weight and frequency. Our Doppler shift group coupling scheme is:

1. For each particle: solve Eq. (62) to modify particle energy weight. For a homologous expansion, the energy weight is multiplied by $e^{-\Delta t_n / t_n}$.
2. For the particle's current cell and group, (j, g), determine the inelastic opacity. If only absorption, then $\sigma_{a,j,g,n}$ is the inelastic opacity.
3. Make a uniformly random sample, $\xi \in [0,1]$.
4. If $\xi \leq \frac{\nu_{g+1/2}}{ct\Delta\nu_g} / (\frac{\nu_{g+1/2}}{ct\Delta\nu_g} + \sigma_{a,j,g,n})$, sample comoving frequency in the group then multiply comoving frequency by $e^{-\Delta t_n / t_n}$. Otherwise, do not sample or redshift comoving frequency.

In the above list, the first step ensures grey outflow radiation diffusion problems are solved correctly (Mihalas & Mihalas 1984, p. 474). If (j, g) only has elastic scattering, then $\nu_{0,p}$ is updated in the same manner as particle energy weight in IMC and DDMC. We constrain source particle frequency to be uniform at the subgroup level; for pure elastic scattering problems, the fourth step above (with uniformly sampled frequency) then emulates the cumulative progression of redshift from elastic scattering in IMC. In the last portion of Section 3, it is found that uniform redistribution in frequency furnishes a grouped transport equation that can be solved without coupling groups with Doppler corrections (see Eqs. (44) and (45)). The fourth step heuristically mitigates frequency shift when redistribution is a strong effect. In terms of Section 3, the condition in the fourth step is similar to $\xi \leq \varepsilon$, where ε is the asymptotic parameter that makes scattering large.

Keeping all terms associated with Doppler shift operator split from the MC solution of Eq. (64) makes opacity regrouping simpler. Moreover, Doppler shifting for non-OR groups in the operator split fashion described is permissible despite use of regrouped groups in Eq. (64). We ensure DDMC particles have a definite non-OR group before and after the MC solution of Eq. (64); this is accomplished by resampling a non-OR group after a leakage or effective scattering event. Equation (63) is solved by advecting DDMC particles with

their velocity cells; cell expansion naturally dilutes radiation energy density.

Following Densmore et al. (2012) and Abdikamalov et al. (2012), DDMC is determined to be applicable to a cell-group by a mean free path threshold, τ_D. Specifically, if the number of mean free paths in a cell-group is greater than τ_D, then the cell-group may apply DDMC. Typical values of τ_D are around 3 to 6 mean free paths per some characteristic cell length (e.g., the minimum length of a rectangular cell). For spherical spatial grids we use the radial length, $\Delta r = t_n \Delta U$. For a three dimensional Cartesian spatial grid, a conservative value might be the minimum of three orthogonal cell lengths. In addition to τ_D, we introduce a mean free path threshold, τ_L, for regrouping groups. This parameter is primarily used for testing solution quality versus degree of opacity regrouping in DDMC. Elastic scattering is not included in computing the mean free paths to check against τ_L since it does not couple DDMC groups. For a DDMC particle, the opacity regrouping algorithm may be delineated as:

1. For each particle: find current cell and group, (j, g), and measure the inelastic collision mean free paths. For absorption, $t_n \Delta U_j \sigma_{a,j,g,n}$ is a measure of effective scattering and effective absorption mean free paths.

2. If $t_n \Delta U_j \sigma_{a,j,g,n} > \tau_L$, then search about g for neighboring groups g_l in cell j satisfying $t_n \Delta U_j \sigma_{a,j,g_l,n} > \tau_L$.

3. For the set of frequencies corresponding to $\cup_l g_l$ where $g \in \cup_l g_l$, apply Eqs. (67), (69), and (70).

4. Perform a DDMC step for each particle to leak into adjacent cell, effectively scatter out of group $\cup_l g_l$, get absorbed, reach census.

5. If not censused, return to first step.

The material temperature field may be updated upon completion of all particle processes. The temperature is updated with Eq. (60) where $f_n \sum_{g=1}^{G} \int_{4\pi} \sigma_{a,g} I_{0,g}$ is estimated with the tallied particle energy deposition.

We obtain luminosity and spectra in the lab frame directly from tallying particles (Lucy 2005). To do so, either a lab frame wavelength grid can be introduced or the comoving wavelength grid can be repurposed as an observational grid in the lab frame. In our scheme, particles are tracked with a lab frame wavelength in IMC; thus determining the group of the IMC particle with a comoving group structure requires a frame transformation. For IMC, a lab frame spectral tally is unambiguous since particle direction, $\hat{\Omega}$, is known. For escaping DDMC particles, we sample direction isotropically at the surface and use the sampled direction to determine the lab frame group of the particle.

7. NUMERICAL RESULTS

In the following calculations, we consider one dimensional spherical problems that test the Gentile-Fleck factor and opacity regrouping in high-velocity outflow. Additionally, Section 7.3 explores mixed weighting in computing group opacities. In the plot legends, "HMC" denotes hybrid Monte Carlo with opacity regrouping (opacity-regrouped IMC-DDMC); "Non-OR HMC" denotes hybrid Monte Carlo without opacity regrouping (non-OR IMC-DDMC). The labels "Standard IMC" and "Standard DDMC" indicate IMC and DDMC solutions that do not apply the modified Fleck factor. For all results shown, source particles and particles undergoing effective scattering have their frequencies uniformly sampled at the subgroup level.

7.1. *Quasi-Manufactured Verification*

Our first problem is a test of the Gentile-Fleck factor using a quasi-manufactured solution (Oberkampf & Roy 2010) for grey transport in a high-velocity outflow. Here, a quasi-manufactured radiation transport solution has an assumed, or manufactured, radiation energy density profile and, in contrast, a material temperature that is solved for using the manufactured radiation energy density and the material equation. The manufactured source term is incorporated in the radiation transport equation to counter redshift and preserve the constancy of the manufactured radiation energy density. For the numerical regime considered, we obtain a positive definite source that is simple to implement. The quasi-manufactured solution provides a benchmark demonstrating that the Gentile-Fleck factor (or modified Fleck factor) provides better accuracy relative to the standard Fleck factor. Specifically, the Gentile-Fleck factor decreases effective absorption, which mitigates potential violations of the IMC Maximum Principle (Larsen & Mercier 1987).

Equation (57) is implemented approximately (Gentile 2011) in an optimized form since computing the derivative of opacity with respect to temperature may be computationally expensive. We use $\partial \sigma_{P,j,n}/\partial T \approx (\sigma_{P,j,n} - (\rho_{j,n}/\rho_{j,n-1})\sigma_{P,j,n-1})/(T_{j,n} - T_{j,n-1})$ for $n \geq 2$, and $\partial \sigma_{P,j,1}/\partial T \approx (\sigma_{P,j}((1+\varepsilon)T_{j,1}) - \sigma_{P,j,1})/(\varepsilon T_{j,1})$ where ε is a user defined parameter. The source term from the manufacturing is positive-definite and yields a solution with non-trivial time dependence. Gentile (2001) provides an analytic solution to a spatially independent problem that is used as a benchmark for modified IMC in static material. The opacity is proportional to T^{-5}, implying that increasing temperature reduces emission. The manufacturing and outflow are an extension of the solution, but we find our analytic result somewhat simpler in form. Assuming pure absorption, integrating the comoving transport equation (Eq. (2)) over frequency, and assuming no spatial dependence yields

$$\frac{\partial E}{\partial t} + \frac{4}{t} E = c\sigma(T)(aT^4 - E) + S_m \quad , \tag{77}$$

and

$$C_v \frac{\partial T}{\partial t} = c\sigma(T)(E - aT^4) \quad , \tag{78}$$

where E is radiation energy density and S_m is the manufactured source. The heat capacity $C_v = \rho c_v$ and the opacity is

$$\sigma(T) = \frac{\kappa \rho}{T^5} \quad , \tag{79}$$

where c_v and κ are constants. We manufacture the radiation field as constant and solve Eq. (78) to obtain a transcendental expression for temperature and time. The manufactured source may then be found from

$$S_m = \frac{4}{t} E + C_v \frac{\partial T}{\partial t} \tag{80}$$

by adding Eqs. (77) and (78). It is clear from Eq. (80) that a monotonically increasing temperature over all time ensures a positive definite source. This should be the case when T

is initialized lower than $(E/a)^{1/4}$. Fortunately a low initial temperature and high initial radiation field is the setup that induces the overheating pathology in standard IMC. Following the approach of Gentile (2011), Eq. (78) may be re-expressed as

$$\left(\frac{(E/a)T}{E/a - T^4} - T\right)\frac{\partial T}{\partial t} = \frac{ac\kappa}{c_v} \tag{81}$$

where conveniently, ρ cancels through division of $\sigma(T)$ by C_v. Equation (81) yields

$$\frac{1}{4}\sqrt{\frac{E}{a}}\ln\left(\frac{[\sqrt{E/a}+T^2][\sqrt{E/a}-T_1^2]}{[\sqrt{E/a}-T^2][\sqrt{E/a}+T_1^2]}\right) - \frac{1}{2}(T^2 - T_1^2) = \frac{ac\kappa}{c_v}(t - t_1) \quad , \tag{82}$$

where t_1 and T_1 are the initial time and material temperature, respectively. For material and radiation properties of interest, Eq. (82), indicates long equilibration time between the fields. Specifically, for an initial radiation temperature of 1.70×10^7 K, an initial material temperature of 1.16×10^5 K, a specific heat capacity of 9.3×10^{17} erg/K/g, and $\kappa = 1.42 \times 10^{35}$ cm^{2}K^5/g, the characteristic equilibrium time is on the order of 10^{91} seconds. These numbers are borrowed or adapted from Gentile (2011). If the scope of simulation time is much smaller, it may safely be assumed that $T^2, T_1^2 \ll (E/a)^{1/2} = T_r^2$ for the numbers given. When the material temperature and initial temperature are much smaller than the radiation temperature, Eq. (82) may be approximated by

$$T(t) = T_r\left[6\frac{ac\kappa}{c_v T_r^2}(t - t_1) + \left(\frac{T_1}{T_r}\right)^6\right]^{1/6} \quad . \tag{83}$$

From Eq. (80), the time integrated manufactured radiation source is approximately

$$\Delta t_n S_{m,n} = \frac{4}{t_n}E\Delta t_n + C_{v,n}(T_{n+1} - T_n) \quad , \tag{84}$$

for small time steps. Equation (84) is positive definite when Eq. (83) is used ($T(t_n) = T_n$).

We construct a problem that induces a "temperature flip" pathology in standard IMC or DDMC. In the first time step, standard IMC-DDMC causes over deposition; this results in the radiation energy density and material temperature respectively dropping and increasing abruptly despite the more gradual nature of the actual solution. Given the strong inverse dependence of opacity on temperature, emission abruptly becomes low, causing the material temperature to remain too high for time spans of interest. Gentile (2011) demonstrates this IMC pathology in the context of static material. Our problem consists of a homologous outflow over 10 spatial cells with a maximum speed of 10^9 cm/s. The material temperature is uniformly initialized to 1.16×10^5 K and the radiation temperature is initialized to the manufactured value of 1.70×10^7 K. Starting from an expansion time of 2 days, we compute the MC results over a 10th of a millisecond, or $t \in [2, 2+1.1574\times10^{-9}]$ days. We test both 100 and 1000 time steps in the time span given. The source, Eq (84), is applied uniformly across the 10 spatial cells. The density is uniform over the spatial domain with a total constant mass of $M = 1 \times 10^{33}$ g. Additionally, $\kappa = 1.42 \times 10^{35}$ cm^{2}K^5/g, $c_v = 9.3 \times 10^{17}$ erg/K/g.

Similar to findings of Gentile (2011), for this test problem it is found that modified pure IMC is very inefficient; the Gentile-Fleck factor increases effective scattering in IMC to a large extent relative to the standard Fleck factor in IMC. Since grey DDMC does not model effective scattering *explicitly*, we test the Gentile-Fleck factor in DDMC; this approach is similar to the use of RW by Gentile (2011) to accelerate a test calculation. In Figure 1, analytic material temperature is calculated with Eq. (83). The MC temperatures are obtained by implementing the manufactured source, Eq. (84), with Eq. (83) used to evaluate T_n and T_{n+1}. For the MC results, the average of the temperature profiles are taken over the 10 spatial cells (temperature change from cell to cell is insignificant, however). Figure 1a has material and radiation temperature results of IMC and DDMC with the standard Fleck factor, and the quasi-manufactured solution versus time. In Fig. 1a, both the IMC and DDMC solutions suffer the "temperature flip" error, in which material temperature becomes non-physically higher than radiation temperature in the first time step. Figure 1b has material and radiation temperature results for DDMC with the modified Fleck factor using 100 (denoted "Large Δt") and 1000 time steps. Results demonstrate the "temperature flip" error is avoided for DDMC modified with the Gentile-Fleck factor. Increasing the number of time steps from 100 to 1000 further improves agreement towards the quasi-manufactured solution. We conclude that the overheating pathology in IMC and DDMC can occur in high-velocity flows and that the Gentile-Fleck factor mitigates the overheating error in high-velocity outflow. However, the ability of the Gentile-Fleck factor to correct the error is apparently limited, since in the early time steps the material temperature becomes too high while the radiation temperature drops too low relative to the analytic solutions.

7.2. *Ten Group Outflow Test*

With 10 group, spherical Heaviside source, outflow problems described by Wollaeger et al. (2013), we test the effect of opacity regrouping in IMC-DDMC for simple yet highly structured opacities. Specifically, we demonstrate the utility of regrouping non-contiguous groups for radiation transport in a high-velocity fluid with astrophysical properties. The approach is described in Section 5 for LTE transport. The form of the opacities is meant to only allow for significant code speed-up when opacities for non-adjacent frequency intervals can be regrouped. With opacity regrouping allowed for non-contiguous group intervals, a DDMC particle has a probability of being in any group that satisfies the regrouping criteria; this generalization improves speed without significant detriment to accuracy relative to the non-opacity-regrouped (non-OR) results for the numerical specifications considered.

The problems consist of a homologous outflow with a maximum outer speed of $U_{\max} = 10^9$ cm/s. The time domain of the problem is $t \in [2, 5]$ days. The temperature of the domain is uniformly initialized to 1.16×10^7 K. There is a uniform radiation source density of $4 \times 10^{24}/t_n^3$ erg/cm^3/s for $|\vec{U}| \in [0, 0.8U_{\max}]$. The source is uniform in frequency as well. The total mass is set to 1×10^{33} g equally divided amongst spatial cells. The heat capacity is $C_v = 2 \times 10^7\rho$ erg/cm^3/K. The groups are spaced logarithmically from 1.2398×10^{-9} cm to 1.2398×10^{-3} cm in wavelength with $g = 1$ being the lowest wavelength group. The opacity in cm^{-1} (with ρ in g/cm^3) is

$$\sigma_{a,g} = \begin{cases} 0.13\rho \quad , & g = 2k-1 \\ 0.13\times10^{-m}\rho \quad , & g = 2k \end{cases} \quad , \tag{85}$$

where $k \in \{1 \ldots 5\}$ and m is set to 4 or 7 (Wollaeger et al.

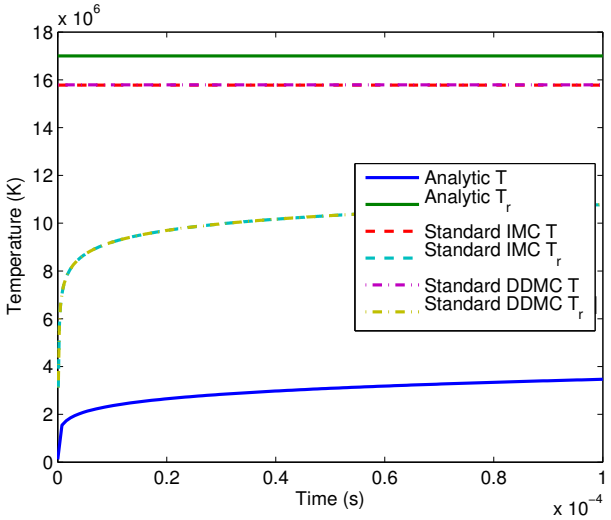

(a)

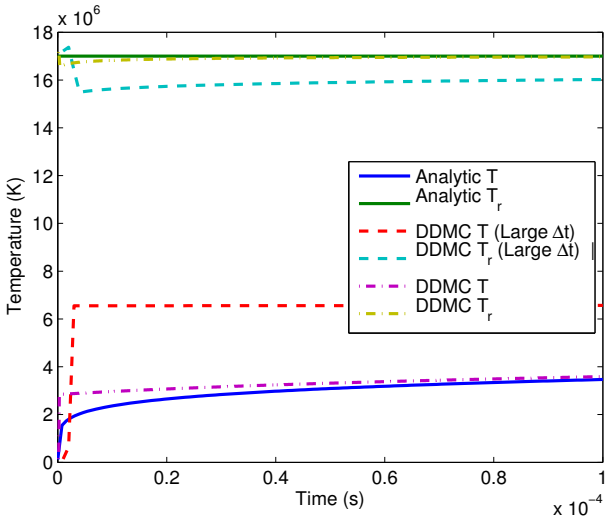

(b)

Figure 1. For the quasi-manufactured problem described in Section 7.1, we compare standard IMC, standard DDMC, and DDMC with the modified Fleck factor against analytic solutions. In Fig. 1a: analytic (solid), standard IMC (dashed), and standard DDMC (dash-dotted) material (T) and radiation (T_r) temperatures for the 1000 time step case. The IMC and DDMC results agree very closely but are both wrong. The IMC (dashed light blue) and DDMC (dash-dotted yellow) radiation temperatures are closer to the analytic material temperature (solid blue) than the analytic radiation temperature (solid green). Inversely, the IMC (dashed red) and DDMC (dash-dotted purple) material temperatures are closer to the analytic radiation temperature than the analytic material temperature. This pathology indicates the standard Fleck factor is insufficient for the time step sizes used. In Fig. 1b: material (T) and radiation (T_r) temperatures from the analytic solution (solid), DDMC with the modified Fleck factor and 100 time steps (dashed, "Large Δt"), and DDMC with the modified Fleck factor and 1000 time steps (dash-dotted). The modified Fleck factor prevents the radiation and material temperatures from "flipping" (see Fig. 1a). Moreover, a decrease in time step size causes further correction of the MC solutions towards the analytic solution.

2013). For both values of m, we use 50 uniform spatial cells, 128 uniform time steps, 0 initial particles, and 100,000 source particles per time step. For all the IMC-DDMC calculations presented, $\tau_L = \tau_D = 3$ mean free paths.

Considering the $m = 4$ disparity, Fig. 2 has radiation energy densities and material temperatures for IMC, non-OR IMC-DDMC, and opacity-regrouped IMC-DDMC; opacity regrouping is not apparently a significant detriment to these solutions. In Fig. 3, the L_1 error for the spectra (in erg/s) of non-OR and opacity-regrouped IMC-DDMC relative to IMC increase while DDMC is dominant and subsequently decrease as outer cells transition to IMC. The DDMC approximation for the lab frame spectral tally becomes steadily less accurate relative to the IMC tally as the cells become optically thin. The influence of opacity regrouping in the $m = 7$ case is similar to that of the $m = 4$ case. In other words the conclusions from Figs. 2 and 3 hold for the $m = 7$ case.

We also incorporate a regrouping cutoff index, g_c, as an experimental parameter. For a group g that meets the regrouping criteria, only groups in the neighborhood $g \pm g_c$ with a number of mean free paths for inelastic collisions greater than τ_L may have their properties used to accelerate the diffusion of particles in g. For $t \in [2, 3.5]$, we test solution speed versus the cutoff group displacement for different regrouping cutoffs, $g_c \in \{0 \ldots 10\}$. Table 1 has times of IMC-DDMC for each g_c value along with the time for IMC. All times presented are for simulation on one core.

Table 1
Run Times for First 64 Time Steps of Heaviside Problem with $g_c \in \{0 \ldots 10\}$ with 1 Core (minutes)

Method	g_c	$m = 4$	$m = 7$
IMC	-	202.23	505.71
HMC	0	23.11	45.09
HMC	1	19.60	37.62
HMC	2	5.80	6.74
HMC	3	5.74	6.71
HMC	4	5.72	6.31
HMC	5	5.79	6.44
HMC	6	5.80	6.41
HMC	7	5.79	6.47
HMC	8	5.83	6.42
HMC	9	5.76	6.54
HMC	10	5.81	6.64

From Table 1, it is evident that regrouping only adjacent groups provides no significant speed up in computation due to the highly non-monotonic structuring of opacity versus group. However, when the regrouping cutoff parameter, g_c, is set to 2, there is a significant reduction in computational cost.

For the problems considered in this section, opacity regrouping in IMC-DDMC is seen to be a large computational advantage without large cost of accuracy to important quantities (spectra and temperatures). For different problems, the control parameters for opacity regrouping may need to be adjusted to maintain good agreement with IMC. To balance efficiency with solution accuracy, adaptive regrouping parameters might be considered. However, for the calculations in the following section, opacity regrouping is constrained to $\tau_D = \tau_L = 3$ with g_c set to the number of groups.

7.3. *W7 Tests*

We now turn to the W7 problem described by Nomoto et al. (1984) and solved by several authors [see, e.g. Kasen et al. (2006); Kromer & Sim (2009); van Rossum (2012)]. The W7 problem consists of simulating radiative transfer in a one dimensional model of Type Ia supernovae. The W7 specifications include density and mass fractions for elements up to Ni

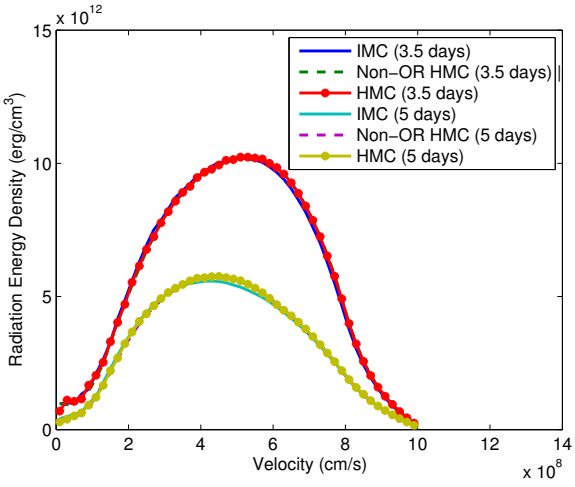

(a)

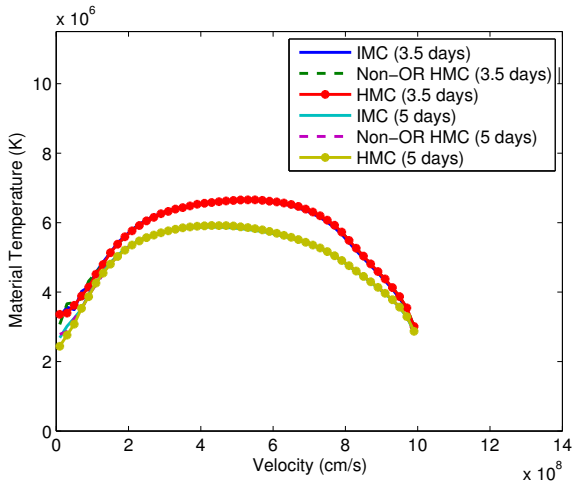

(b)

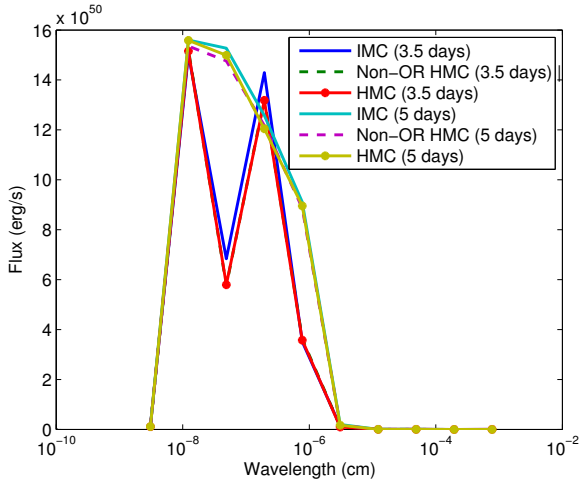

(c)

Figure 2. Radiation energy density, material temperature, and grouped spectra of IMC (solid), non-opacity-regrouped (non-OR) IMC-DDMC (dashed, $g_c = 0$), and opacity-regrouped IMC-DDMC (dot-solid, $g_c = 10$) at 3.5 and 5 days for the 10 group, outflow problem with a spherical Heaviside source described in Section 7.2. Radiation energy density and material temperature are plotted versus fluid velocity and spectra are plotted at group wavelength centers. The opacity is described by Eq. (85) with $m = 4$. In Figs. 2a, 2b, and 2c, radiation energy density, material temperature, group spectra, respectively. For this problem, the IMC-DDMC results with opacity regrouping show good agreement with the non-OR results.

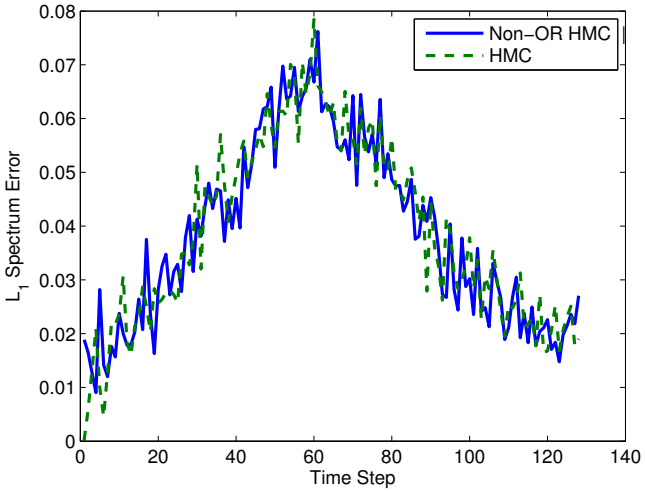

Figure 3. Non-opacity-regrouped (non-OR) IMC-DDMC (solid), and opacity regrouped IMC-DDMC (dashed) L_1 error versus time step of group spectra relative to pure IMC for radiation escaping the outermost cell of the 10 group, Heaviside source problem described in Section 7.2. The opacity is described by Eq. (85) with $m = 4$. The spectral error for both non-OR and opacity-regrouped IMC-DDMC progressively increases relative to IMC until pure IMC is applied in the outer cells. Error from opacity regrouping appears insignificant relative to error from DDMC.

on a velocity grid. The radial outflow speed at the outer boundary is ∼7% of the speed of light. In the free-expansion phase of the supernova radioactive decay of ^{56}Ni heats the fluid and causes it to radiate in the UV, visible and infrared ranges of the spectrum. For this problem, we apply the modified Fleck factor, tested in Section 7.1, and opacity regrouping, tested in Section 7.2. Additionally, we test different calculations of the grouped opacity by introducing uniform subgroups for each group. Despite the physical and algorithmic complexities of the opacity, IMC-DDMC yields light curves and spectra that are in good agreement with those of `PHOENIX` for the numerical specifications considered. Moreover, the total computation times are on the order of hours (see Table 2).

For IMC-DDMC, a method that in our formulation requires a group structure, the W7 problem has the difficulty of requiring many groups for accurate spectra. Specifically, we find that the number of groups required to achieve a resolved light curve is on the order of thousands. While IMC-DDMC is easily extensible to 2 and 3 spatial dimensions in theory, storing ∼10,000 groups per spatial cell is expensive in memory. Apart from memory overhead, there is the difficult question of spectral accuracy. In particular, it may be advantageous to implement adaptive group bounds so that important portions of the spectrum are properly resolved; no part of the theory presented precludes adaptive wavelength bounds or even non-uniform group number per cell. In this section, we focus mainly on the performance of IMC-DDMC with opacity regrouping. We test the effect of mixing reciprocal (Rosseland) and arithmetic (Planck) computations of the opacity on light curves and spectra. Additionally, we show that spikes in the temperature profile at late time are mitigated with the Gentile-Fleck factor. However, the application of the Gentile-Fleck factor reveals uncertainty in the spectra around day 6 post-explosion for the numerical set-up presented. For the following simulations, the code `SuperNu` is run on 192 cores on the Cray XE6 supercomputer Beagle at the Computation Institute of the University of Chicago.

In each time step, the opacity per group is computed using a subgroup structure to allow for non-trivial opacity profile weighting. Opacity contributions to each group include bound-bound (bb), bound-free (bf), and free-free (ff) transitions. Unless otherwise specified, groups are spaced logarithmically while subgroups are treated uniformly. Additionally, there is a grey scattering opacity that is isotropic in the comoving frame calculated as (Castor 2004, p. 161)

$$\sigma_s = \frac{8\pi}{3} n_{e^-} \left(\frac{e^-}{m_{e^-} c^2} \right)^2 \quad , \tag{86}$$

where e^- is electron charge, n_{e^-} is electron number density, and m_{e^-} is electron mass in cgs units. With mass fractions known *a priori* and given the assumption of LTE, the Saha-Boltzmann equations are used to obtain the excitation densities for each atom in the W7 model (Mihalas & Mihalas 1984, p. 49). To calculate opacity, we introduce a subgrid for each group g with index $g_g \in \{1 \dots G_g\}$. Values for bb opacities are calculated from oscillator strength data for each atomic species (Kurucz 1994). Furthermore, it is assumed that a line is entirely included in the subgroup its line center is located. So (Mihalas & Mihalas 1984, pp. 329-332),

$$\begin{aligned} \sigma_{a,g_g,bb} = & \\ & \frac{1}{\Delta\lambda_{g_g}} \sum_s \sum_i \sum_{i'>i} \left(\frac{\pi (e^-)^2}{m_{e^-} c} \right) f_{i,i',s} \frac{\lambda_{i,i',s}^2}{c} \times \\ & [\Theta(\lambda_{i,i',s} - \lambda_{g_g - 1/2}) - \Theta(\lambda_{i,i',s} - \lambda_{g_g + 1/2})] \times \\ & n_{i,s} (1 - e^{\frac{hc}{kT\lambda_{i,i',s}}}) \quad , \end{aligned} \tag{87}$$

where $\sigma_{a,g_g,bb}$ is the bb contribution to subgroup g_g, $f_{i,i',s}$ is the non-dimensional oscillator strength from state i to i' of species s, $\lambda_{i,i',s}$ is the wavelength center of the line corresponding to the $i \rightarrow i'$ transition, $n_{i,s}$ is the total density of species s occupying state i, and the Θ are Heaviside step functions constraining the sum to opacity profiles centered in the subgroup. The bound-free opacities are tabulated according to the analytic fit prescription of Verner et al. (1996). We approximate the bf opacity, $\sigma_{a,g_g,bf}$, of the subgroup as the value of the fit at the center wavelength in the subgroup. The ff opacities, $\sigma_{a,g_g,ff}$, are computed with tabulated Gaunt factors based on the work of Sutherland (1998) and are similarly evaluated in the subgroup. The total absorption opacity for subgroup g_g is $\sigma_{a,g_g} = \sigma_{a,g_g,bb} + \sigma_{a,g_g,bf} + \sigma_{a,g_g,ff}$ (Mihalas & Mihalas 1984, p. 332). The total group opacity may then be averaged in some manner over the sub group contributions. We introduce an opacity mixing control parameter $\alpha_\sigma \in [0, 1]$ to linearly combine reciprocal ("Rosseland type") and direct averages of opacity. Averages of reciprocal opacity may preferentially weight lower opacity. For instance, Rosseland opacity is lower than Planck opacity. For some weight function, $w(\lambda)$, the group absorption opacity is calculated as

$$\begin{aligned} \sigma_{a,g} = (1 - \alpha_\sigma) \frac{1}{w_g} \sum_{g_g}^{G_g} \sigma_{a,g_g} \int_{\lambda_{g-1/2}}^{\lambda_{g+1/2}} w(\lambda) d\lambda + \\ \frac{\alpha_\sigma w_g}{\sum_{g_g}^{G_g} \sigma_{a,g_g}^{-1} \int_{\lambda_{g-1/2}}^{\lambda_{g+1/2}} w(\lambda) d\lambda} \quad , \end{aligned} \tag{88}$$

where $w_g = \int_{\lambda_{g-1/2}}^{\lambda_{g+1/2}} w(\lambda) d\lambda$. For a uniform weight function, Eq. (88) simplifies to

$$\sigma_{a,g} = (1 - \alpha_\sigma) \frac{1}{G_g} \sum_{g_g}^{G_g} \sigma_{a,g_g} + \frac{\alpha_\sigma G_g}{\sum_{g_g}^{G_g} 1/\sigma_{a,g_g}} \quad . \tag{89}$$

If LTE is considered, the weight function might be set to the normalized Planck function; in this case Eq. (88) is a mix of grouped Planck and Rosseland opacities.

For the W7 tests discussed, gamma ray energy deposition profiles and the initial material and radiation temperatures are borrowed from the PHOENIX code (Hauschildt 1992; Hauschildt & Baron 1999; Hauschildt & Baron 2004; van Rossum 2012). We estimate and apply a nominal value of heat capacity of $C_v = 2.0 \times 10^7 \rho$ erg/K/cm^3 from Pinto & Eastman (2000) to compute the Fleck factor and update the material temperature. It has been found that changing C_v by a factor of 3 does not change temperatures and spectra; the insignificance of C_v is attributable to the disparity of energy storage between the radiation and material fields. In the W7 problem, the Fleck factor is found to be very small in IMC and IMC-DDMC. Consequently, even a modest group resolution in IMC causes effective scattering to dominate particle processes. For the W7 tests attempted, it is apparently unfeasible to use pure IMC, non-OR IMC-DDMC, or even IMC-DDMC where opacity regrouping is limited to adjacent groups. For a 100 group W7 simulation with groups logarithmically spaced from 1×10^{-6} cm to 3.2×10^{-4} cm, 64 velocity cells spaced uniformly from 0 cm/s to 2.2027×10^9 cm/s, a time domain of $t \in [40, 64]$ days post explosion with 0.25 day time steps, 250,000 initial particles, and 250,000 source particles per time step, neither IMC nor non-OR IMC-DDMC completed the simulation with 192 cores and a wall time of 40 hours each. In contrast, fully opacity-regrouped IMC-DDMC ($g_c = 100$) completed the same problem with 24 cores in 1018.9 seconds. For the scope of this paper, we focus our attention to opacity-regrouped IMC-DDMC simulations.

Our first W7 test problems explore the effect of different group opacity averaging and group resolution. Specifically, Eq. (89) is implemented. The problems considered have 225, 400, 625, and 1024 groups, 20 subgroups per group, and an opacity mixing parameter $\alpha_\sigma \in \{0.0, 0.3, 0.5, 0.8, 1.0\}$. Each calculation has 64 velocity cells uniformly spaced from 0 cm/s to 2.2027×10^9 cm/s, 248 uniform time steps for $t \in [2, 64]$ days, 250,000 initial radiation particles, 250,000 source particles generated per time step, $\tau_D = \tau_L = 3$ mean free paths, and the opacity-regrouped neighborhoods span the entire set of groups ($g_c = G$). Absolute bolometric magnitudes are calculated with

$$M_{\text{bol}} = 4.74 - 2.5 \log_{10} \left(\frac{L}{3.84 \times 10^{33}} \right) \quad , \tag{90}$$

where L is luminosity in erg/s. The luminosities are computed by tallying lab frame particle energies escaping the domain and dividing by time step size. Figures 4a, 4b, 4c, and 4d have light curves calculated with Eq. (90) for $G = 225$, $G = 400$, $G = 625$, and $G = 1024$, respectively, and a fixed number of subgroups, $G_g = 20$. Similarly Figs. 5a, 5b, 5c, and 5d have spectra at 20 days post explosion calculated with Eq. (90) for $G = 225$, $G = 400$, $G = 625$, and $G = 1024$, respectively, and $G_g = 20$. For the group resolutions presented, the $\alpha_\sigma = 1.0$ case does not appear to converge at the same rate as the other results. In other words, the $\alpha_\sigma = 1.0$ case for Eq. (89) produces more sensitivity in brightness and spectrum versus

course group resolutions. As the mixing parameter is increased towards 1, the opacity calculation applies more reciprocal averaging. Since reciprocal averaging favors smaller subgroup opacity values, it is expected that larger α_σ yield earlier and brighter light curves. Despite producing unrealistic light curves for $\alpha_\sigma \approx 1$, α_σ may be calibrated between 0 and ~ 0.3 to make simulations with low or modest group numbers emulate high-resolution simulations.

Table 2 has computation times for each curve. Timing results for the problem described are for 24 cores. With source particle numbers kept constant, simulation time scales sub-linearly with increasing group number.

Table 2
Total Run Times for Opacity-Regrouped HMC W7 with 24 Cores (hours)

$G \setminus \alpha_\sigma$	0.0	0.3	0.5	0.8	1.0
225	0.92	0.92	0.91	0.89	0.83
400	1.33	1.32	1.32	1.28	1.21
625	1.92	1.88	1.91	1.87	1.89
1024	2.73	2.71	2.70	2.70	3.32

We now examine the effect of the Gentile-Fleck factor, or Eqs. (54) and (58) along with the optimization described in the last paragraph of Section 7.1, on W7 temperatures. Figure 6 has spectra and material temperature profiles shown at day 3 and 32 post-explosion for the W7 problem described with $\alpha_\sigma = 0.5$ and $G = 225$. At early times ($t \lesssim 10$ days), both IMC-DDMC and modified IMC-DDMC yield outer-cell temperature fluctuations for the numerical specifications considered. The fluctuations are different between the standard and modified methods. Consequently, the application of the Gentile-Fleck factor in IMC-DDMC uncovers some uncertainty in early spectra. At later times ($t \gtrsim 25$ days), the Gentile-Fleck factor yields consistently smoother material temperature profiles than the standard Fleck factor. However, the spectra at later times are not significantly affected by the fluctuations in the outer-cell temperatures because that region is optically thin at that point.

Finally, we compare the results of SuperNu and PHOENIX for the W7 problem in LTE. We find that the light curve generated by SuperNu is systematically ∼10% dimmer at peak than the light curve generated by PHOENIX for various time step and group resolutions. For controlled testing, grouped opacities have been introduced into PHOENIX. The multigroup computations have no opacity mixing, or $\alpha_\sigma = 0$. Figure 7 has 500 group light curve results from PHOENIX and SuperNu along with a standard, high-resolution (30,000 wavelength points) PHOENIX light curve. From inspection of Fig. 7b, it is worth noting that the luminosities of *multigroup* PHOENIX and SuperNu have similar early rising light curves. This means that the different diffusion treatments in the two codes are in good agreement. The standard PHOENIX light curve rises earlier than the multigroup PHOENIX light curve, as expected. This effect can be emulated in low group resolution simulations using the opacity mixing parameter (see Figure 4). Increasing α_σ from 0 to ~ 0.3 has a similar effect on the light curve shape as increasing the resolution to convergence. Figure 8 has spectra at 10, 20, and 40 days post-explosion for the 500 group SuperNu and high-resolution PHOENIX simulations. Despite differences in magnitudes, the time evolution of the light curves and the shapes of the spectra are in good agreement. The codes use the same atomic data but the EOS and opacity routines are different; these factors may account for some differences in the luminosities and spectra.

Resolving the sources of the 10-15% discrepancy will require more in-depth code-to-code comparisons which is work in progress but beyond the scope of this paper. Having performed time step and group resolution tests, we also plan to perform resolution tests on the spatial grid. It is possible the codes have different convergence properties with grid resolution. In particular, the standard leakage opacity at IMC-DDMC spatial method interfaces may underpredict particle transmission across cell surfaces when DDMC interface cells are optically thick (Densmore et al. 2007). Densmore et al. (2006) performs an emissivity based derivation to generalize the standard IMC-DDMC boundary condition and improve the emission from DDMC to IMC at spatial interfaces. If increased grid resolution in SuperNu increases the luminosity, then the alternate boundary condition presented by Densmore et al. (2006) may increase the absolute bolometric magnitude of the light curve at the current 64 cell resolution. We have performed preliminary tests with an emissivity based boundary condition and find a ∼2% increase in the absolute bolometric magnitude at peak; despite this modest change, exploring the effects of increasing the spatial resolution may be revealing. Apart from grid resolution, EOS, opacities, and transport methods, there may be other important reasons for the observed differences.

8. CONCLUSIONS AND FUTURE WORK

We have incorporated techniques to mitigate overheating errors and combine DDMC groups with high opacity in the IMC-DDMC code, SuperNu. In Section 6, we described an approach to Doppler shift DDMC particles. The Doppler shift scheme accounts for the effect of inelastic collisions with uniform subgroup redistribution. Following Abdikamalov et al. (2012), the Doppler shift scheme is operator split from the diffusion scheme; it does not conflict with the opacity regrouping process.

We found that opacity regrouping is needed in IMC-DDMC to make the W7 problem feasible; the optimization mitigates computational cost in performing the multidimensional calculation. Additionally, we have described and tested an approach to treating the opacity that involves refining the wavelength grid to subgroups.

In Section 7.1 we used the Gentile-Fleck factor to mitigate an overheating pathology in the presence of strong outflow. The MC results are benchmarked against a quasi-manufactured solution. In Section 7.2, we treated structured multigroup problems with IMC-DDMC to test the effect of non-contiguous opacity regrouping. For the problem presented, opacity regrouping significantly improves efficiency without a significant cost of accuracy in the temperatures and spectra. In Section 7.3, we tested IMC-DDMC with opacity regrouping and subgrouping on the W7 problem. We also compared light curves and spectra for the W7 test problem calculated using SuperNu and PHOENIX for a similar set-up. We modified PHOENIX to be able to use multigroup opacities, which enabled us to do more controlled code-to-code comparisons. The light-curve rise times given by multigroup PHOENIX and SuperNu are in good agreement for the same group resolution. We find satisfactory agreement in the shape of the spectra. However, there exists a ∼10-15% discrepancy between SuperNu and PHOENIX in the luminosity of the light curve around and after peak that is currently not fully understood. Time step resolution tests indicate the light curves compared between codes

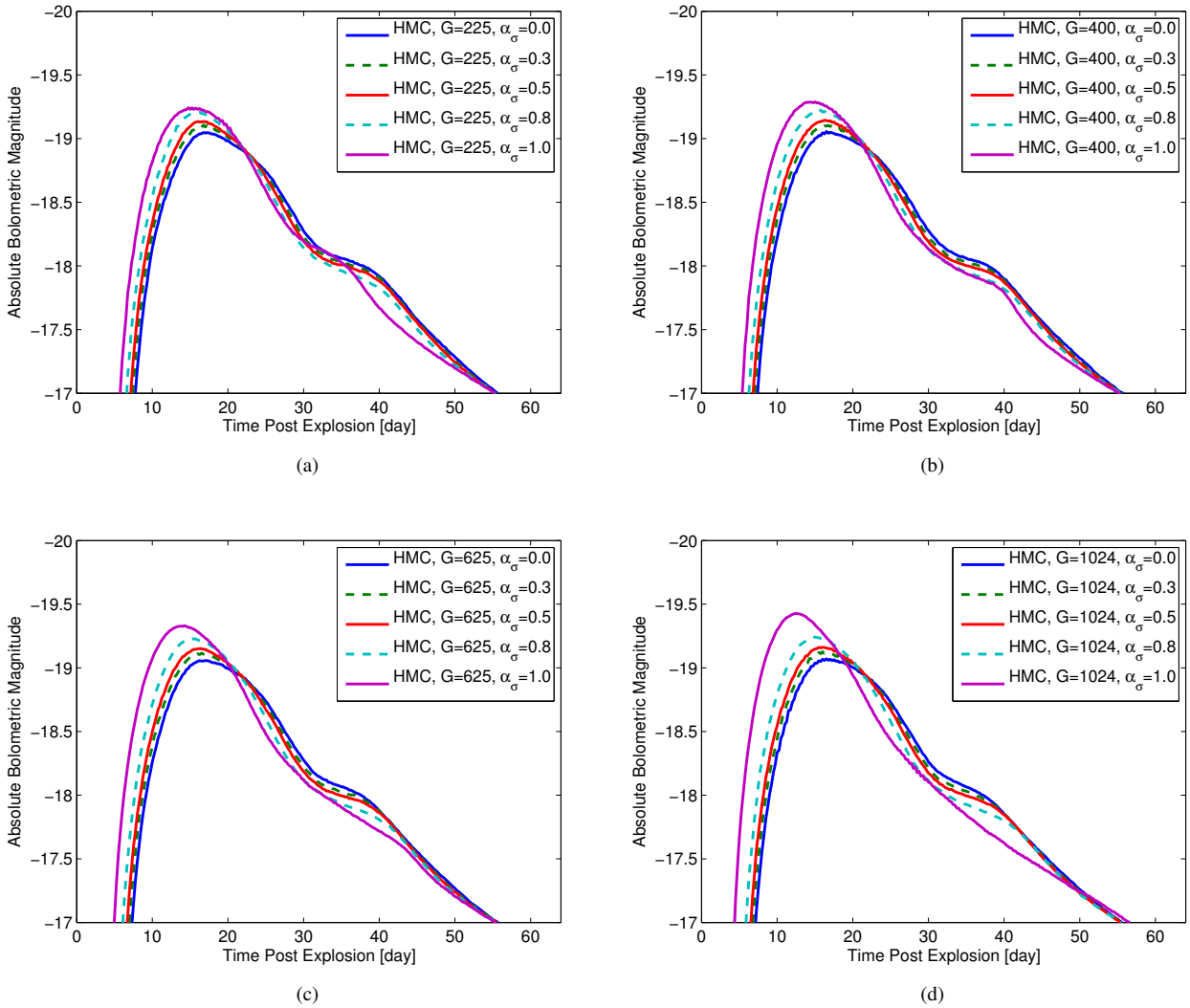

Figure 4. Opacity-regrouped IMC-DDMC W7 bolometric light curves for opacity mixing $\alpha_\sigma \in \{0.0, 0.5, 1.0\}$ (solid) and $\alpha_\sigma \in \{0.3, 0.8\}$ (dashed; so solid and dashed curves alternate versus α_σ) and a fixed number of subgroups, $G_g = 20$. Equation (89) has been applied for opacity mixing. Light curves are calculated by tallying particles that have escaped the spatial (velocity) domain per time step and applying Eq. (90). In Figs. 4a, 4b, 4c, and 4d group resolutions are $G = 225$, $G = 400$, $G = 625$, and $G = 1024$, respectively. As expected, peak luminosity is earlier and brighter for opacity mixing that favors reciprocal averaging since smaller subgroup opacity values are favored. Values of α_σ close to 1 are not realistic as opacities of strong absorption lines are more and more neglected. The opacity mixing parameter can be used to calibrate simulations with modest group resolution to emulate the diffusion characteristics of equivalent high-resolution simulations.

are converged in time. For certain spatial grid resolutions, DDMC may underpredict spatial leakage of diffusion particles to IMC (Densmore et al. 2006, 2007). Consequently, spatial grid resolution tests of `SuperNu` may be informative.

We plan to extend our code to multiple dimensions. The IMC-DDMC method is simple to extend to two and three dimensions for simple grid geometries. The challenges in performing multidimensional simulations of SN Ia light curves and spectra with IMC-DDMC lies in optimization and memory requirements. In addition to spatial geometry, we plan to investigate methods and algorithms that further mitigate spurious temperature spikes due to the Maximum Principle or MC noise.

9. ACKNOWLEDGEMENTS

We would like to thank Donald Lamb, Gregory Moses, and Carlo Graziani for supporting and guiding this work. We would like to thank Donald Lamb for the constructive recommendations and suggestions. We especially thank our referee, Ernazar Abdikamalov, for the valuable recommendations that improved this paper. This research was supported in part by the NSF under grant AST-0909132, and by NIH through resources provided by the Computation Institute and the Biological Sciences Division of the University of Chicago and Argonne National Laboratory, under grant S10 RR029030-01. This work is supported in part at the University of Chicago by the National Science Foundation under grant PHY-0822648 for the Physics Frontier Center "Joint Institute for Nuclear Astrophysics" (JINA).

REFERENCES

Abdikamalov, E., Burrows, A., Ott, C. D., Loffler, F., O'Connor, E., Dolence, J. C., & Schnetter, E. 2012, ApJ, 755, 111
Adams, M. L. 2001, Nucl. Sci. Eng., 137
Atzeni, S., & ter Vehn, J. M. 2004, The Physics of Inertial Fusion (Oxford University Press)

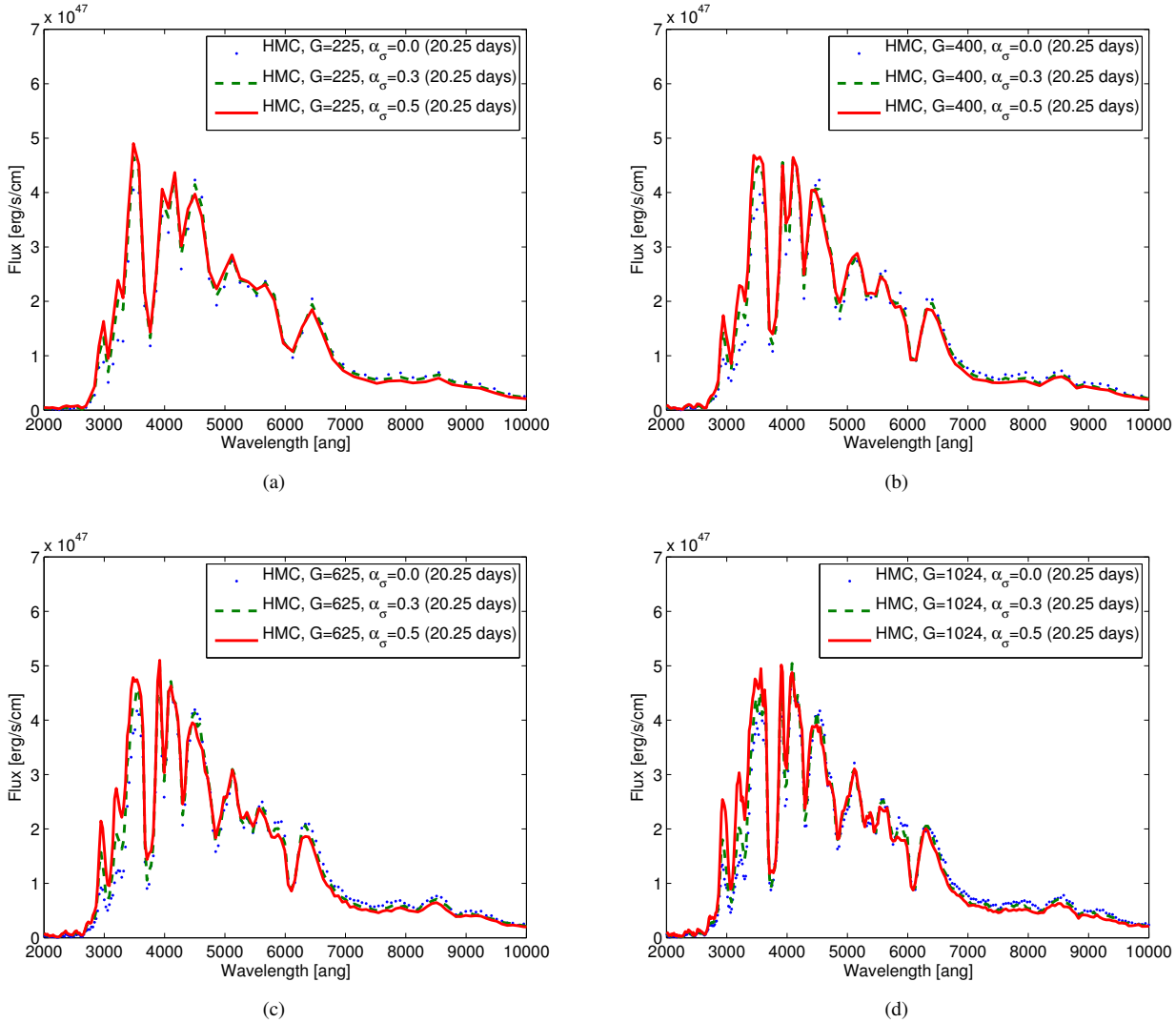

Figure 5. Opacity-regrouped IMC-DDMC W7 spectra for opacity mixing $\alpha_\sigma = 0.0, 0.3, 0.5$ (dotted, dashed, and solid, respectively) and a fixed number of subgroups, $G_g = 20$. Equation (89) has been applied for opacity mixing. Spectra are calculated by tallying escaping particles energies per group per time and dividing by group wavelength range. Data are plotted at group centers. In Figs. 5a, 5b, 5c, and 5d group resolutions are $G = 225$, $G = 400$, $G = 625$, and $G = 1024$, respectively. Locations of peaks and troughs amongst the different opacity mixings presented appear consistent. For $\lambda \in [2000, 4000]$, radiation transmission is larger for larger values of α_σ.

Baron, E., & Hauschildt, P. H. 2007, A&A, 468, 255
Branch, D., & Khokhlov, A. 1995, Physics Reports, 256, 53
Brooks, E. D. 1989, J. Comput. Phys., 83
Buchler, J. R. 1983, JQSRT, 30, 395
Calder, A. C., Plewa, T., Vladimirova, N., Lamb, D. Q., & Truran, J. W. 2004, Astrophysical Journal, Letters
Calder, A. C., et al. 2002, Astrophysical Journal, Supplement, 143, 201
Carter, L. L., & Forest, C. A. 1973, lA-5038, Los Alamos National Laboratory
Castor, J. I. 2004, Radiation Hydrodynamics (Cambridge University Press)
Cleveland, M. A., & Gentile, N. 2014, Transport Theory and Statistical Physics, 1
Cleveland, M. A., Gentile, N. A., & Palmer, T. S. 2010, J. Comput. Phys., 229, 5707
Densmore, J. D. 2011, J. Comput. Phys., 230, 1116
Densmore, J. D., Davidson, G., & Carrington, D. B. 2006, Ann. Nucl. Energy, 33, 583
Densmore, J. D., Evans, T. M., & Buksas, M. W. 2008, Nucl. Sci. Eng., 159, 1
Densmore, J. D., & Larsen, E. W. 2004, J. Comput. Phys., 199, 175
Densmore, J. D., Thompson, K. G., & Urbatsch, T. J. 2012, J. Comput. Phys., 231, 6925
Densmore, J. D., Urbatsch, T. J., Evans, T. M., & Buksas, M. W. 2007, J. Comput. Phys., 222, 485
Fleck, Jr., J. A., & Canfield, E. H. 1984, J. Comput. Phys., 54, 508
Fleck, Jr., J. A., & Cummings, J. D. 1971, J. Comput. Phys., 8, 313
Fryxell, B., et al. 2000, ApJS, 131, 273
Gamezo, V. N., Khokhlov, A. M., Oran, E. S., Chtchelkanova, A. Y., & Rosenberg, R. O. 2003, Science, 299, 77
Gentile, N. A. 2001, J. Comput. Phys., 172, 543
—. 2011, J. Comput. Phys., 230
Habetler, G. J., & Matkowsky, B. J. 1975, J. Math. Phys., 16, 846
Hauschildt, P. H. 1992, JQSRT, 47, 433
Hauschildt, P. H., & Baron, E. 1999, Journal of Computational and Applied Mathematics, 109
Hauschildt, P. H., & Baron, E. 2004, A&A, 417, 317
Hauschildt, P. H., & Wehrse, R. 1991, JQSRT, 46
Hillebrandt, W., & Niemeyer, J. 2000, ARA&A, 38, 191
Kasen, D., Thomas, R. C., & Nugent, P. 2006, ApJ, 651, 366
Kromer, M., & Sim, S. A. 2009, Mon. Not. R. Astron. Soc., 398
Kurucz, R. L. 1994
Larsen, E. W., & Mercier, B. 1987, J. Comput. Phys., 71
Lewis, E. E., & Miller, Jr., W. F. 1993, Computational Methods of Neutron Transport (American Nuclear Society)
Long, M., et al. 2013, ArXiv e-prints
Lowrie, R. B., Mihalas, D., & Morel, J. E. 2001, JQRST, 69, 291
Lucy, L. B. 2005, A&A, 429, 19
Malvagi, F., & Pomraning, G. C. 1991, J. Math. Phys., 32, 805
McClarren, R. G., Holloway, J. P., & Brunner, T. A. 2008a, JQSRT, 109, 389
McClarren, R. G., Lowrie, R. B., Prinja, A. K., & Morel, J. E. 2008b, JQSRT, 109, 2590
McClarren, R. G., & Urbatsch, T. J. 2009, J. Comput. Phys., 228, 5669

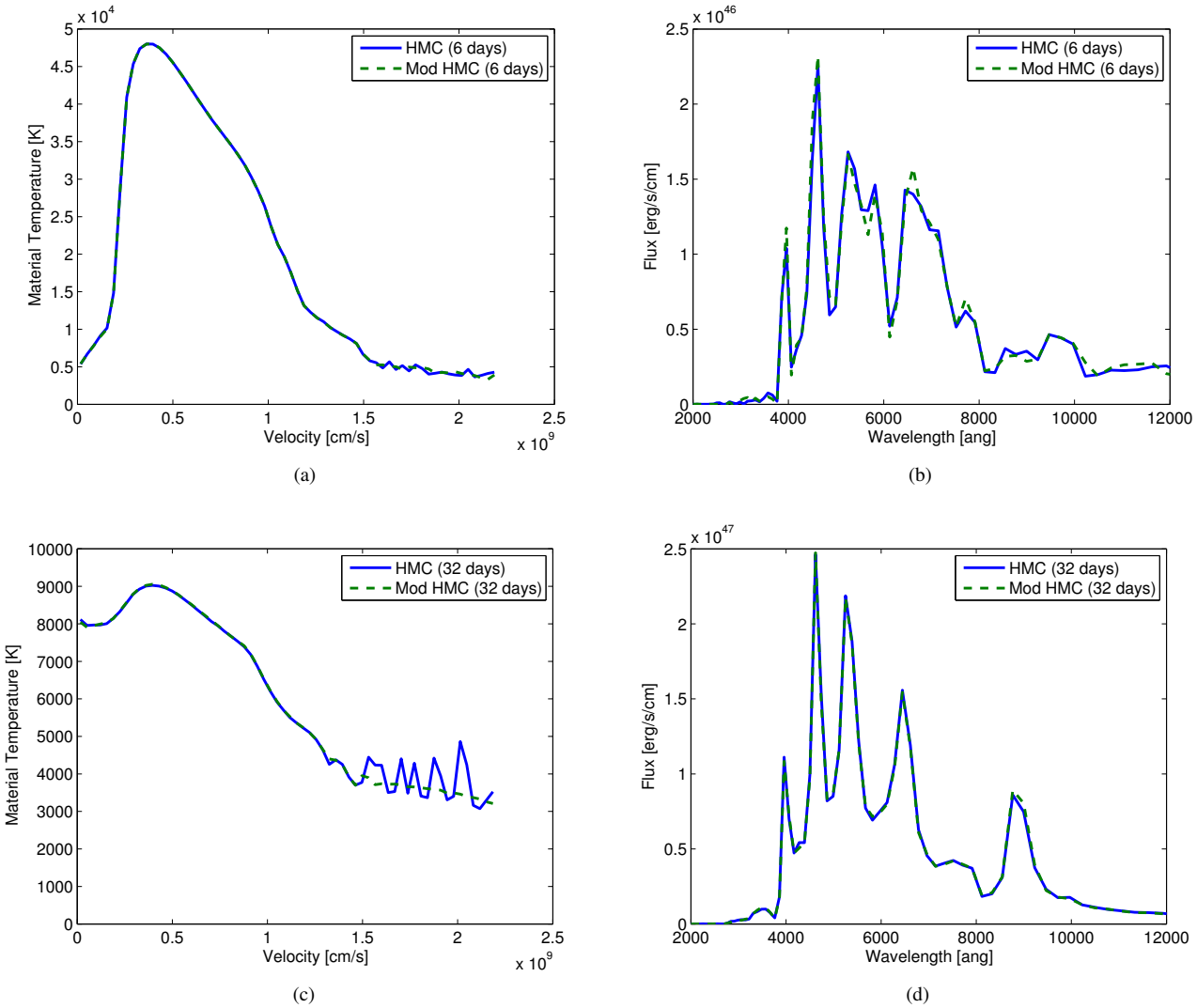

Figure 6. IMC-DDMC (solid) and Gentile-Fleck factor modified IMC-DDMC (dashed) material temperatures (left) and spectra (right) at days 6 and 32 post-explosion for the W7 problem described in Section 7.3 with $G = 225$ and $\alpha_\sigma = 0.5$. At early time ($t \lesssim 10$ days), the Gentile-Fleck factor slightly modifies the spectrum which is sensitive to its effect on the fluctuations in the outer regions of the ejecta. At late times in the W7 expansion ($t \gtrsim 25$ days), the Gentile-Fleck factor consistently mitigates temperature fluctuations in the outer cells. Despite the continued temperature fluctuations in the outer cells for standard IMC-DDMC at later times, the difference in spectra at late times is no longer significant.

McClarren, R. G., & Urbatsch, T. J. 2012, in Transactions of the American Nuclear Society

McKinley, M. S., Brooks, E. D., & Szőke, A. 2003, J. Comput. Phys., 189, 330

Mihalas, D., & Mihalas, B. W. 1984, Foundations of Radiation Hydrodynamics (Oxford University Press)

N'Kaoua, T. 1991, SIAM J. Stat. Comput., 12, 505

Nomoto, K., Thielemann, F., & Yokoi, K. 1984, ApJ, 286, 644

Oberkampf, W. L., & Roy, C. J. 2010, Verification and Validation in Scientific Computing (Cambridge University Press)

Olson, G. L., & Kunasz, P. B. 1987, JQSRT, 38

Perlmutter, S. 2003, Physics Today, 53

Perlmutter, S., et al. 1999, ApJ, 517, 565

Petschek, A. 1990, Supernovae (Springer-Verlag)

Phillips, M. M. 1993, ApJ, 413, L105

Pinto, P. A., & Eastman, R. G. 2000, ApJ, 530, 744

Pomraning, G. C. 1973, The Equations of Radiation Hydrodynamics (Pergamon Press)

Riess, A. G., et al. 1998, AJ, 116, 1009

Scannapieco, C., Tissera, P. B., White, S. D. M., & Springel, V. 2008, MNRAS, 389

Seitenzahl, I. R., et al. 2013, MNRAS, 429, 1156

Su, B., & Olson, G. L. 1999, JQSRT, 62, 279

Sutherland, R. S. 1998, MNRAS, 300

Szőke, A., & Brooks, E. D. 2005, JQSRT, 91, 95

Urbatsch, T. J., Morel, J. E., & Gulick, J. C. 1999, in Proc. Int. Conf. Mathematics and Computation, Reactor Physics, and Environment Analysis in Nuclear Applications

van Rossum, D. R. 2012, ApJ, 756, 31

Verner, D. A., Ferland, G. J., Korista, K. T., & Yakovlev, D. G. 1996, ApJ, 465

Warsa, J. S., & Densmore, J. D. 2010, Nucl. Sci. Eng., 166, 36

Wollaeger, R. T., van Rossum, D. R., Graziani, C., Couch, S. M., Jordan, G. C., Lamb, D. Q., & Moses, G. A. 2013, ApJS, 209

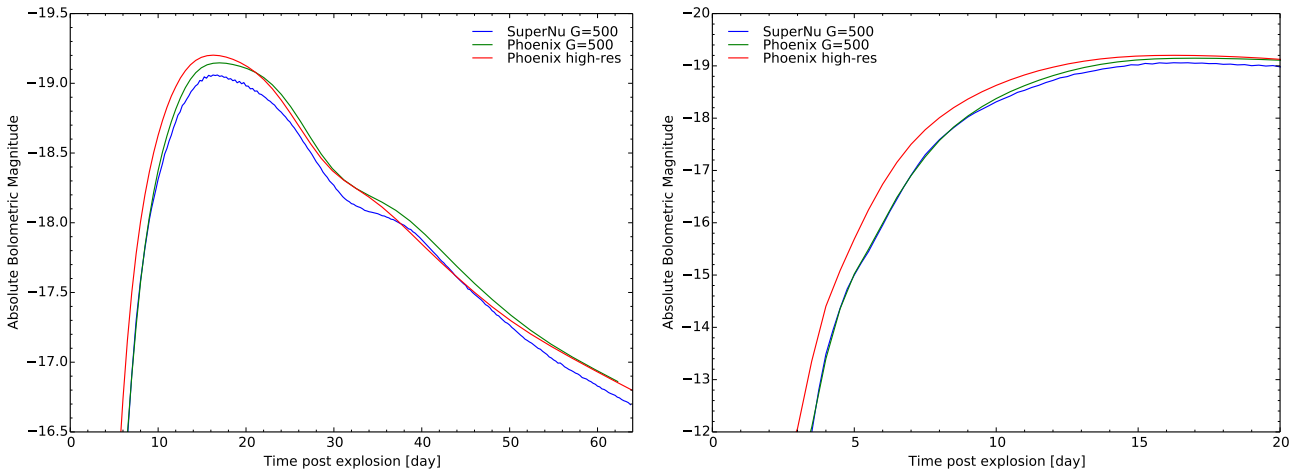

(a) (b)

Figure 7. SuperNu (blue), with multigroup PHOENIX (green), and standard PHOENIX (red) light curves. SuperNu and multigroup PHOENIX apply 500 groups and directly averaged group opacity, or an $\alpha_\sigma = 0$ mix. PHOENIX is run in LTE for consistency with SuperNu. There exists a systematic difference of $\sim$10-15% in luminosity for much of the W7 evolution between the multigroup results. Differences in transport, EOS, or opacity routines along with spatial grid resolution may account for some of the discrepancy. In Fig. 7b, it is notable that the multigroup results give very similar early rising light curves, meaning that the different diffusion treatments in the two codes are in good agreement. The standard PHOENIX light curve rises earlier than multigroup PHOENIX. This is due to the high resolution that enables windows of lower opacity through which diffusion is enhanced. Diffusion at low group resolutions can be simulated and calibrated using the opacity mixing parameter α_σ (see Figure 4).

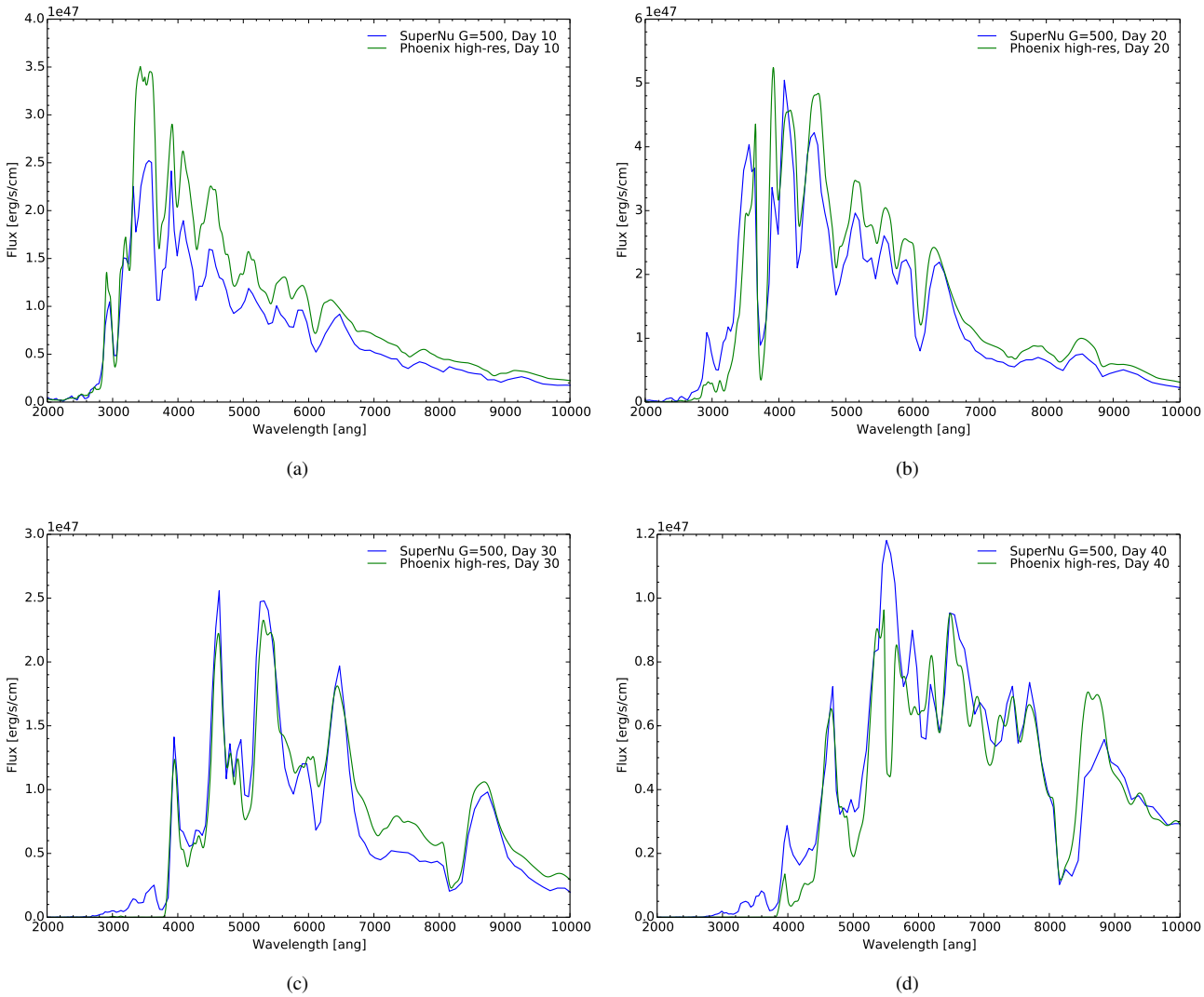

Figure 8. `SuperNu` (blue) with 500 groups and standard `PHOENIX` (green) spectra for the W7 problem at 10, 20, 30, and 40 days post-explosion. In Fig. 8a, the difference in flux is partly attributable to the earlier rise of the `PHOENIX` high-resolution luminosity (see Fig. 7). In Fig. 8b, the W7 supernova is near peak luminosity; resolving the discrepancy in flux requires further code-to-code comparison. In Fig. 8d, the flux of `PHOENIX` is not systematically larger than `SuperNu`. Around day 40, the high-resolution `PHOENIX` light curve is at a lower luminosity than the 500 group `SuperNu` light curve. Given the considerable differences in computational methods between the codes, the temporal behavior and shape of the spectra are in good agreement.